

Surface Deformation and Seismicity Linked to Fluid Injection in the Raton Basin

by

Cameron Chambers

B.S., Virginia Polytechnic and State University

A Thesis Submitted to the  
Faculty of the Graduate School of the  
University of Colorado Boulder  
In partial fulfillment of the  
Requirements for the degree of  
Master of Science  
Department of Geological Sciences

2023

Committee Members:

Dr. Shemin Ge

Dr. Kristy Tiampo

Dr. Anne Sheehan

## **Abstract**

Chambers, Cameron (M.S., Geological Sciences)

Surface Deformation and Seismicity Linked to Fluid Injection in the Raton Basin

Thesis directed by Professor Shemin Ge

It is suggested that deep fluid injection may cause surface uplift and subsidence in oil and gas producing regions in addition to seismicity. This study uses the Raton Basin as an example to investigate the hydromechanical processes of surface uplift and subsidence following fluid injection and relate them to the region's seismic history. The Raton Basin, in southern central Colorado and northern central New Mexico, has experienced wastewater injection related to coalbed methane and gas production starting in 1994 and increased seismicity since 2001. In this study, we estimate the extent and magnitude of total vertical deformation in the Raton Basin from 1994 to 2020, and short-term deformation between the years 2017 to 2020 following a sharp decline in injection rates. Most modeled uplift between 1994 and 2020 occurred near the southern wells, where the greatest cumulative volume of wastewater was injected. However, modeled subsidence occurred around the southern and eastern wells between 2017 and 2020, after the rate of injection decreased. This shows that while the magnitude of uplift corresponds to cumulative injection volume and maximum rate in the long-term, short-term incremental deformation (uplift or subsidence) is controlled by changes in the rate of injection. The increased number of yearly earthquake events follow periods of modeled rapid uplifting throughout the basin, suggesting that surface deformation is caused by the same injection induced pore pressure perturbations that initiate seismicity.

## Acknowledgements

I would like to thank several key individuals who have been instrumental in helping me reach this point in graduate school. First, I would like to express my gratitude to my advisor, Shemin Ge, for her guidance and support throughout my research journey over the past two years. Her keen attention to detail, unwavering support, and dedication to high quality inspired me to strive for the highest standards in my graduate work and beyond. I am grateful to my committee members, Kristy Tiampo and Anne Sheehan, for their valuable feedback, expert advice, and thought-provoking questions that have helped me develop my research approach and interpretations. My lab group, including Fabiana Fuentes, Scott Stokes, and Claudia Corona, fostered an intellectually stimulating, supportive, and fun environment where I could learn and grow as a hydrogeologist. I am grateful for their support, camaraderie, friendship, and entertaining conversations that kept me going through the ups and downs. I would also like to thank my research counterparts, Megan Brown, Scott Stokes, and Elizabeth Menezes for their collaboration, shared knowledge, and contributions to my work. Finally, my friends and family have been a steadfast source of support and encouragement throughout my entire academic journey. I am deeply grateful for their unwavering belief in me, their patience and understanding during the challenging moments of graduate school, and their celebration of my achievements. I would especially like to thank my parents and sister. I wouldn't be who I am today without you.

Funding for this work was provided in part by the United States Department of Energy grant DE-SC0020222.

# Table of Contents

1. Introduction .....	1
1.1. Surface Deformation: A <i>poroelastic</i> effect of fluid injection.....	1
1.2. Fluid Induced Seismicity in the United States .....	4
2. Geologic Setting and Background .....	5
2.1 The Raton Basin.....	5
2.2 History of Wastewater Injection in the Raton Basin .....	9
2.3 Study Objectives and Research Questions.....	11
3. Modeling Methodology.....	11
3.1 Hydrostratigraphy Model Development.....	12
3.2 Groundwater Flow Modeling.....	13
3.3 Surface Deformation Calculation.....	13
4. Results.....	14
4.1 Long-term Deformation 1994-2020.....	14
4.2 Short-term Deformation 2017-2020.....	18
5. Discussion .....	21
5.1 Pore Pressure Distribution and Surface Deformation.....	21
5.2 Surface Deformation and Earthquake Occurrence .....	22
5.3 Why is there subsidence in the South and East? .....	23
5.4 Additional Mechanisms Impacting Surface Deformation .....	25
6. Conclusion.....	27
References .....	29
Appendix A: Detailed Modelling Methodology .....	36

A.1. Injection Well Data.....	36
A.2. Pore Pressure Modeling .....	37
A.3 Surface Deformation Modeling .....	44
Appendix B: First-order lithospheric expansion estimation .....	53
B.1 Coalbed Methane and Gas Production and Mining Activities.....	53
B.2 Lithospheric Expansion Due to Groundwater Storage Depletion .....	56
Appendix C: Sensitivity Analysis .....	58
Appendix D: Recent DInSAR interpretations of Surface Deformation and Future Work. ....	61
D.1 Differential Interferometric Synthetic Aperture Radar (DInSAR).....	61
D.2 Interpreted surface deformation using DInSAR .....	63
D.3 Future work: Pore Pressure Model Calibration using DInSAR interpretations .....	65
Appendix E: Additional Data Tables .....	67

## Tables

<b>Table A-1:</b> Hydrogeologic parameters used in study.....	41
<b>Table C-1:</b> Parameters used in sensitivity analysis.....	58
<b>Table E-1:</b> Injection well information.....	67
<b>Table E-2:</b> Injection well coordinates.....	69
<b>Table E-3:</b> Earthquake data.....	70
<b>Table E-4:</b> Monthly injection rates for wells in the East (1994-2020).....	78
<b>Table E-5:</b> Monthly injection rates for wells in the South (1994-2020).....	93
<b>Table E-4:</b> Monthly injection rates for wells in the West (1994-2020).....	115
<b>Table E-4:</b> Monthly injection rates for wells in the North (1994-2020).....	130

## Figures

<b>Figure 1.</b> Conceptual diagram of injection induced uplift.....	3
<b>Figure 2.</b> Map of the Raton Basin including the locations of injection wells.....	6
<b>Figure 3.</b> Raton Basin stratigraphy.....	8
<b>Figure 4.</b> Time series of cumulative regional injection rates.....	10
<b>Figure 5.</b> Map of modeled long-term (1994-2020) deformation.....	15
<b>Figure 6.</b> Time series of modeled vertical deformation and recorded magnitude 3 or greater earthquakes.....	17
<b>Figure 7.</b> Maps of modeled short-term (2017-2020) and incremental deformation.....	19
<b>Figure 8.</b> Comparison of deformation and injection time series for the South and East.....	24
<b>Figure A-1.</b> Simplified diagram depicting hydrostratigraphy model development.....	38
<b>Figure A-2.</b> Aerial and cross-sectional view of model domain.....	39
<b>Figure A-3.</b> Pressure change distribution for 2017 and 2020.....	43
<b>Figure A-4.</b> Diagram depicting surface deformation calculation.....	49
<b>Figure B-1.</b> Map of Raton Basin mining and oil/gas production.....	54
<b>Figure B-2.</b> Time series of extracted water related to oil/gas production.....	55
<b>Figure C-1.</b> Sensitivity analysis results.....	60
<b>Figure D-1.</b> Conceptual diagram depicting Differential Interferometric Synthetic Aperture Radar (DInSAR) measurements of surface displacements due to injection.....	62
<b>Figure D-2.</b> Map of surface deformation in the Raton Basin between 2017 and 2020 interpreted using DInSAR.....	64

# 1. Introduction

## 1.1. Surface Deformation: A *poroelastic* effect of fluid injection

Surface deformation can occur surrounding Class II injection wells, where briny wastewater produced during oil and gas production is disposed into the deep rock formations (e.g., Shirzaei et al, 2016; Shirzaei et al, 2019; Deng et al, 2020; Brown et al., 2022). The deformation observed at the surface reflects poroelastic stress changes surrounding injection (Teatini et al. 2011), where perturbations in pore pressure can expand or contract the porous aquifer material (**Figure 1**). This is a concept in poroelasticity that describes the coupling between deformation of a porous medium and the changes in pore fluid pressure. The theory of poroelasticity describes two basic processes: 1.) *Solid to fluid coupling* takes place when stress is applied to a porous medium, deforming the material and altering the pore pressure regime, and 2.) *Fluid to solid coupling* occurs when the fluid pressure increases or decreases in the pores of the medium, causing the material to deform (Wang, 2000). Fluid pressure perturbations within the pores of the rock can induce stress changes in the surrounding rock matrix, causing the rock to deform (Detournay et al., 1993; Wang, 2000). Cumulative elastic deformation in the subsurface can be observed at the surface as positive vertical surface deformation or negative vertical surface deformation. In this study, we refer to positive vertical surface deformation as uplift and negative as subsidence.

The surface deformation can be inferred using geodetic techniques such as differential interferometric synthetic aperture radar (DInSAR). Previous studies have reported uplift on the order of millimeters to centimeters near wastewater disposal sites (e.g., Shirzaei et al. 2016;

Barba-Sevilla et al. 2018; Kim and Lu 2018; Loesch and Sagan 2018; Deng et al., 2020; Brown et al., 2022). In some cases, subsidence has been observed near high-rate injectors (e.g., Deng et al., 2020), though the reason this occurs is not fully understood. It has been suggested that deformation can be related to fluid injection (e.g., Deng et al., 2020), but quantitative support through modeling is lacking.

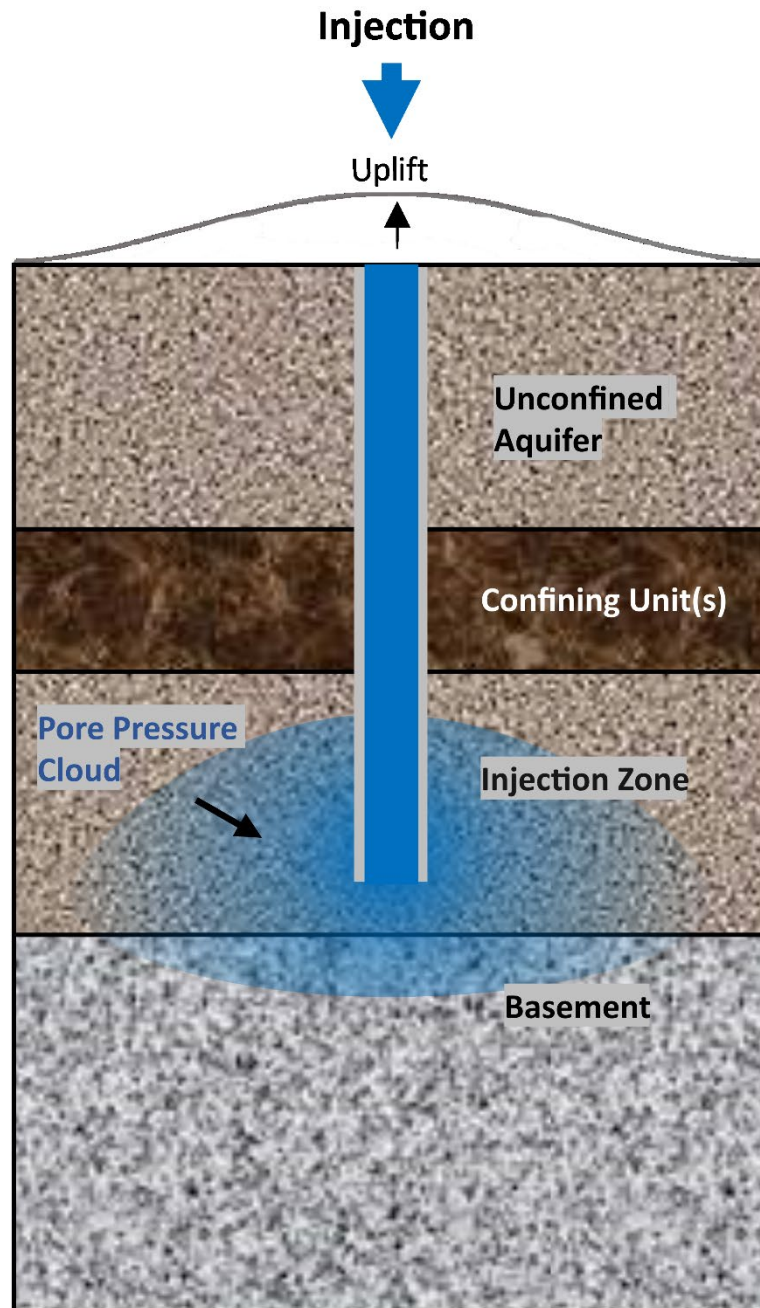


**Figure 1:** Conceptual Diagram representing surface uplift due to deep wastewater injection. Fluid injected into the aquifer can increase the pore pressure surrounding injection. Increased pressure can cause the rock to deform, often creating an observable signal at the surface.

## 1.2. Fluid Induced Seismicity in the United States

Some oil and gas producing regions in the mid-continental United States, an area historically seismically inactive, have experienced a glaring increase in the number of recorded earthquakes over the past several decades (Ellsworth, 2013). Multiple studies have associated the uptick in seismic events to the increased rate of deep wastewater injection (e.g. Davis & Frohlich, 1993; Horton, 2012; Weingarten et al., 2015; Kim & Lu, 2018; Pollyea et al., 2018). Roughly 10% of all class II injection wells in the United States, where briny wastewater produced during oil and gas production is disposed into the deep stratigraphy, are clearly associated with increased seismic activity (Weingarten et al., 2015). Class II wastewater injection has been shown to create sufficient stress perturbations along nearby fault zones that can initiate seismicity (Zhang et al., 2013; Keranen et al., 2014; Hornbach et al., 2015; Brown et al., 2017; Goebel et al., 2017). As fluid is injected, it increases the pore pressure in the aquifer where, over time, the pore pressure diffuses outward from the injection interval (Ge and Saar, 2022). When significant pore pressure accumulates along a critically stressed fault, often located in the crystalline basement rock, increased pore pressure causes a decrease in normal stress which can lead to slip (Hubbert and Rubey, 1959; Healy et al., 1968; Stokes, 2022.; Ge and Saar, 2022). Studies have shown that a pressure increase of as little as 0.01 to 0.1 MPa is sufficient to cause failure along a critically stressed fault (Reasenberg and Simpson, 1992; Stein, 1999; Stokes, 2022). Elastic stress changes due to fluid injection experienced at critically stressed faults can increase the likelihood and rate of induced seismicity when combined with pore pressure perturbations (e.g. Zhai et al., 2019) or can even be considered the dominant

triggering mechanism when there is little hydraulic connectivity between the injection interval and earthquake nucleation point (e.g. Chang and Segall, 2016; Goebel et al., 2017).

## 2. Geologic Setting and Background

### 2.1 The Raton Basin

The Raton Basin located in southern central Colorado and northern central New Mexico has experienced wastewater injection related to coalbed methane and gas production starting in 1994 (Colorado Oil and Gas Conservation Commission [COGCC], 2020; New Mexico Oil Conservation Division [NMOCD], 2020). Beginning with the 2001 earthquake sequence near Trinidad, CO, the Raton Basin has also had an uptick in the number of earthquakes associated with wastewater injection (Rubinstein et al., 2014; Nakai et al., 2017). This sequence occurred in the northern portion of the Trinidad Fault Zone shown in **Figure 2** (Stokes et al., 2023). A notable earthquake sequence occurred along the Trinidad fault zone a second time in 2011 which nucleated in the southern portion of the fault zone. This sequence included a magnitude 5.3 earthquake, the largest recorded earthquake in the Basin's recorded history (Stokes et al., 2023). The magnitude of completeness (the magnitude threshold for which all earthquakes can be detected) for the years 2001 – 2014 in the Raton Basin was determined to be 3.0 (Rubinstein et al., 2014). Stokes et al. (2023) modeled the pore pressure change due to injection within the Raton Basin and found that pore pressure change accumulated along several fault zones within the region and was sufficient to trigger seismicity. However, how the surface deforms in the Raton Basin in response to pore pressure changes from wastewater injection has never been modeled.

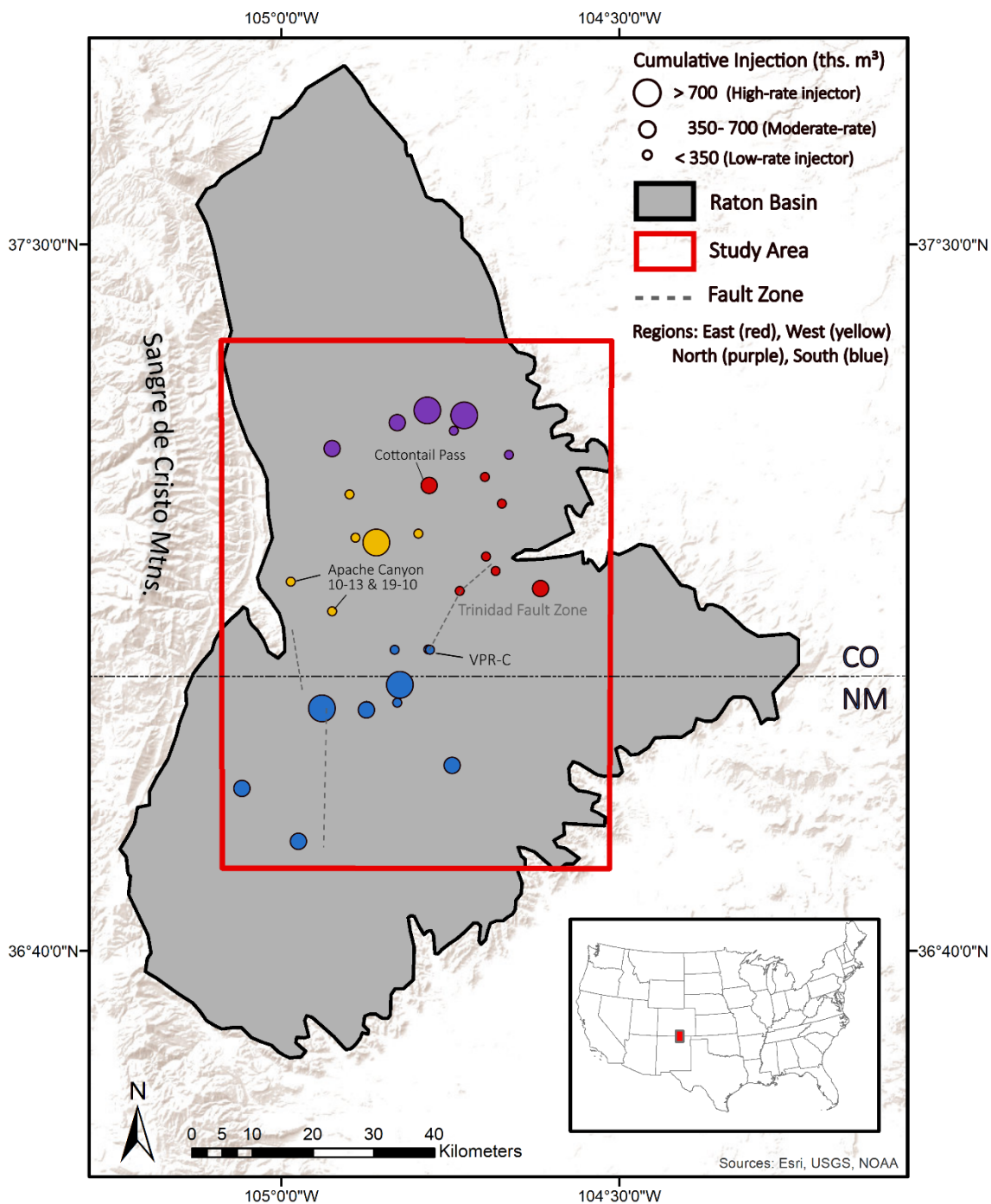


**Figure 2.** Map of the Raton Basin including locations of injection wells. The symbol sizes correspond to total volume of injected fluid (1994-2020) and are colored by geographic region; East (red), West (yellow), North (purple), and South (blue). The first well in operation was Cottontail Pass well in 1994, shortly followed by the Apache Canyon 10-13 and 19-10 wells in the West region. The first injection well in operation in the south is the VPR-C. In 2001, the first fluid induced earthquake sequence occurred along the Trinidad fault zone. A second notable earthquake occurred along the Trinidad Fault zone in 2011 that included the largest earthquake in the Raton Basin’s recorded history.

A total of twenty-nine injection wells have operated within the Raton Basin between 1994 and 2020 (**Figure 2**). Injection began in Colorado in November of 1994, and the first well in New Mexico began operation in 1999 (COGCC 2020, NMOCD 2020). The average depth of injection is roughly 2-3km, and mainly in the permeable Dakota Sandstone formation (**Figure 3**) (COGCC 2020; NMOCD 2020; Stokes, 2022). The injection interval underlies the kilometer thick Pierre Shale, a low permeability confining unit acting as a hydraulic barrier separating the injection formation from the upper stratigraphy (Baltz, 1965). Beneath the primary injection interval, separating it from the Pre-Cambrian basement rocks, are multiple moderately permeable to permeable Permian-Pennsylvanian basal sedimentary units; the Morrison, Dockum, and Sangre De Cristo formations, respectively (Baltz, 1965; Weingarten, 2015; Nakai et al., 2017)

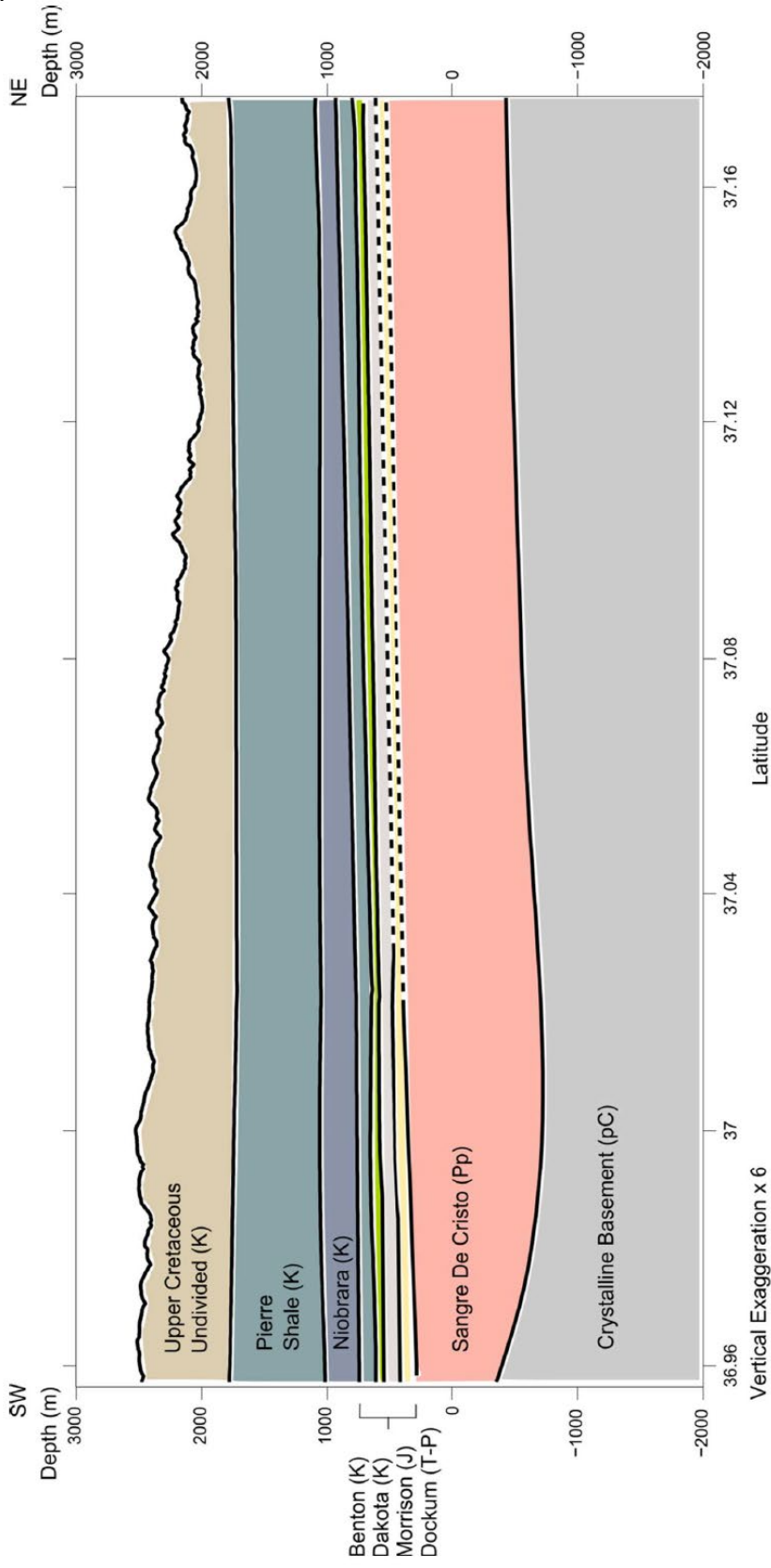


**Figure 3.** Cross-sectional view of the Raton Basin stratigraphy oriented from southwest to northeast (from Weingarten, 2015). “K” refers to Cretaceous, “J” means Jurassic, “T-P” denotes Triassic to Permian, and “pC” denotes Pre-Cambrian aged rock. Wastewater is injected into permeable sandstone formations beneath the Pierre Shale, mainly targeting the Dakota sandstone, and is hydraulically disconnected from surficial aquifers.

## 2.2 History of Wastewater Injection in the Raton Basin

To better understand how injection rate and volume affects the extent and magnitude of deformation, we categorize each of the 29 injection wells by geographic region within the Raton Basin study area: East, West, North, and South (**Figure 2**). The first well in operation is the Cottontail Pass well, located in the East, which began injecting in November of 1994. It was soon joined by two high-rate injection wells in the West; Apache Canyon 10-3 and Apache Canyon 19-10 (COGCC, 2020). Both wells began operation in January of 1995. Between 1994 and the early 2000s, most of the injection occurred in the East and West (**Figure 4**). In 1999, the first injection well in New Mexico, VPR-A, began operation (NMOCD, 2020). By the early 2000s, the southern portion rapidly overtook the eastern and western areas in terms of total monthly injection rate. The southern portion of the study area continued to experience the greatest amount of injection through the year 2020. The rate of injection in the south continued to increase until its peak in 2014. Beginning in 2014 there was a rapid decline in the rate of injection within the southern portion of the study area, though the cumulative rate of injection in the south remained higher than the other regions. The eastern region reached peak injection rate in the early 2000's, then has trended downwards through 2020. The western and northern sections have experienced a general increase in injection rate between 1994 and 2020.

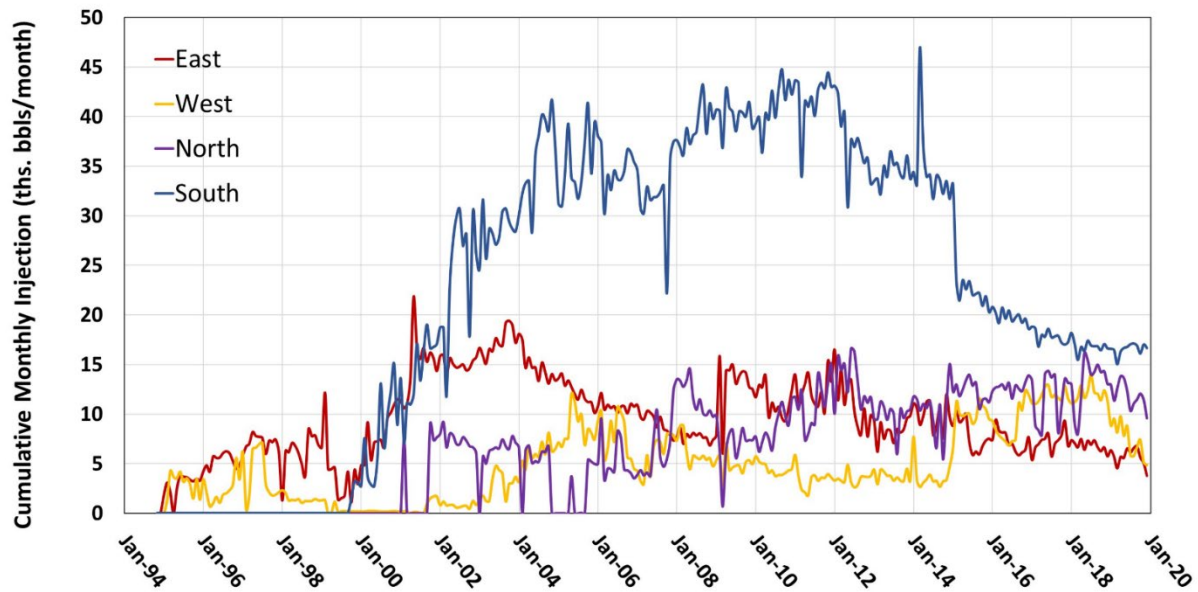


**Figure 4:** Time series of cumulative monthly injection rate for the four regions within the Raton Basin (COGCC, 2020; NMOCD, 2020). The eastern and western regions saw the earliest injection but was quickly overtaken by the southern wells in the early 2000s. After 2014, the south experienced a sharp decrease in injection rate. Rates in the east have been steadily declining since the early 2000s.

This region is a suitable location for this study due to its history of class II injection and subsequent fluid induced seismicity. Basin-scale pore pressure perturbations due to wastewater injection between 1994-2020 in the Raton Basin was modeled by Stokes et al (2023) which show sufficient pressure change along faults to initiate seismicity. To what degree wastewater injection contributes to surface deformation, however, is uncertain. Geodetic techniques, such as differential interferometric synthetic aperture radar (DInSAR), can measure total surface deformation due to the combination of potentially multiple co-occurring mechanisms including fluid injection. However, it cannot determine the magnitude or extent of deformation related to any specific process unless other processes are factored out.

Deformation can likely be caused by fluid injection (Teatini et al., 2011) or withdrawal (e.g., Barnhart et al., 2014) and other anthropogenic activities, erosional processes such as landslides (e.g. Notti et al., 2015), earthquake slip (e.g. Atzori et al., 2009, Barnhart et al., 2014), and aseismic creep (e.g. Tiampo, 2013). To relate surface deformation, pore pressure diffusion, and increased seismicity, it is imperative that we quantify and constrain the contribution of wastewater injection to surface deformation.

### **2.3 Study Objectives and Research Questions**

The role wastewater injection plays in causing the deformation remains uncertain. Furthermore, it is unclear if surface deformation is related to injection induced pore pressure perturbations that caused seismicity. The objective of this study is to examine how the surface may deform in response to wastewater injection in the Raton Basin through time. More specifically, we examine the poroelastic effects of pore pressure changes due to increases and decreases in injection rates in different regions of the Basin. The following are two specific research questions.

- 1.) What is the extent and magnitude of regional surface deformation caused by wastewater injection wells in the Raton Basin, and how does it respond to varying rates of injection?
- 2.) Is surface deformation related to pore pressure perturbations that initiated seismicity?

## **3. Modeling Methodology**

To address these questions, we estimate the extent and magnitude of long-term total vertical deformation in the Raton Basin from 1994 since injection began to 2020, and short-

term incremental deformation between the years 2017 to 2020 by using a multifaceted modeling approach. We utilize MODFLOW-2005 (Harbaugh et al., 2005) to model the pore pressure propagation due to wastewater injection between 1994 and 2020 (Stokes, 2022). We then use the relation developed by Brown et al. 2022 to calculate surface deformation using the change in hydraulic head. Finally, we analyze the extent and magnitude of surface deformation and compare our calculated time-series of surface deformation to number of yearly earthquake occurrences.

The modeling methodology utilized for this research is outlined here in three primary steps; 1.) Hydrostratigraphy model development, 2.) Groundwater Flow Modeling, and 3.) Surface Deformation Calculation. More detailed information on methodology can be found in **Appendix A.**

### **3.1 Hydrostratigraphy Model Development**

For this study, we use a 3-dimensionally discretized basin scale hydrostratigraphy model of the Raton Basin developed by Stokes et al. (2023). The model is made up of three primary hydrostratigraphic units encompassing the upper stratigraphy, target injection formations, and basement and it incorporates topography. It includes the geographic location, screen intervals (the part of the well where wastewater enters the targeted aquifer), and monthly wastewater injection rates for all 29 injection wells between 1994 and 2020. Stokes et al. (2023) provides a more detailed explanation of hydrostratigraphy model development.

### 3.2 Groundwater Flow Modeling

The distribution of hydraulic head change due to fluid injection in the Raton Basin was modeled by solving the governing equation for groundwater flow using MODFLOW (Harbaugh et al., 2005). The governing equation for groundwater flow in 3-dimensions is as follows.

$$\frac{\partial}{\partial x} \left( K_{xx} \frac{\partial h}{\partial x} \right) + \frac{\partial}{\partial y} \left( K_{yy} \frac{\partial h}{\partial y} \right) + \frac{\partial}{\partial z} \left( K_{zz} \frac{\partial h}{\partial z} \right) + \sum_{n=1}^N Q_n(t) \delta(x - x_n) \delta(y - y_n) \delta(z - z_n) = S_s \frac{\partial h}{\partial t} \quad (1)$$

where  $h$  is hydraulic head (L),  $S_s$  is the specific storage ( $L^{-1}$ ),  $K_{xx}$ ,  $K_{yy}$ ,  $K_{zz}$  are the principle components of the hydraulic conductivity tensor ( $L T^{-1}$ ),  $x$ ,  $y$ ,  $z$  are spatial coordinates,  $t$  is time (T),  $\delta$  is the Dirac delta function ( $L^{-1}$ ),  $Q_n$  is the injection rate for well  $n$ , and  $N$  is the number of injection wells.

Hydraulic head ( $h$ ) is related to pore pressure through the following relation:

$$h = \frac{p}{\rho_f g} + h_z \quad (2)$$

where  $p$  ( $ML^{-1}T^{-2}$ ) is pore pressure,  $\rho_f$  is fluid density,  $g$  ( $L T^{-2}$ ) is gravitational acceleration, and  $h_z$  (L) is the elevation head.

### 3.3 Surface Deformation Calculation

To calculate surface deformation, we apply the method of Brown et al. (2022) using the groundwater flow model results of hydraulic head over time. The method relates vertical surface deformation to the change in hydraulic head ( $\Delta h$ ) as follows:

$$D(i, j, t) = \sum_{k=1}^N S_{S_k} b_k \Delta h_k \quad (3)$$

where  $D(i, j, t)$  (L) is the total surface deformation at the discretized model index location  $i, j$  and time  $t$  (T), expressed as the sum of the change in vertical thickness of  $N$  model layers with individual layer index  $k$ .  $S_{S_k}$  is the specific storage and  $b_k$  is the thickness of layer  $k$ .  $\Delta h_k$  is the hydraulic head change in layer  $k$  over a time step. The model assumes that deformation is entirely vertical, elastic, and instantaneous (described in detail in **Appendix A**). The surface deformation results were examined in areal views and time-series are created for four locations.

## 4. Results

Our modeled surface deformation estimates indicate both positive and negative vertical surface deformation occurring at various times throughout the study area. Results for 1994 – 2020 representing long-term deformation and 2017-2020 representing short-term deformation are examined.

### 4.1 Long-term Deformation 1994-2020

Most of the total modeled deformation between 1994 and 2020 occurred near the southern wells, where the highest rate of injection occurred, and the greatest total volume of wastewater was injected. The model shows significant calculated total uplift in the eastern portion of the study area as well. Some modeled uplift occurred in the northern and western region of the study area, though to a lesser degree. Between 1994 and 2020, the maximum

modeled uplift was around 14.7 cm. An aerial view of modeled surface deformation in the long-term is shown in **Figure 5**.

Between 1994 and 2020, uplift greater than 3 cm occurred over an area of around 1100 km<sup>2</sup> and uplift greater than 6 cm occurred over an area of nearly 150 km<sup>2</sup>. An area of nearly 9

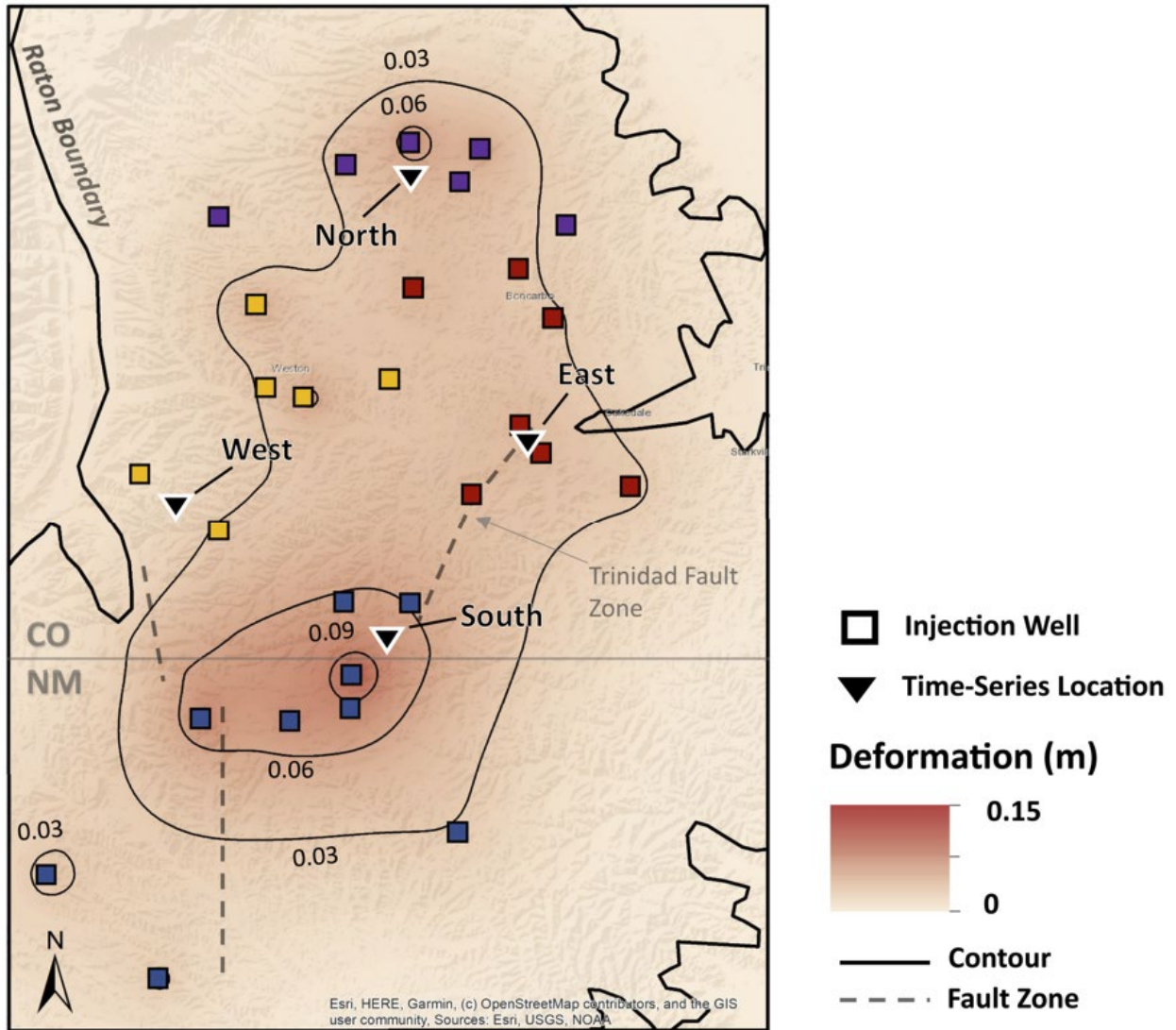


**Figure 5.** Mapped model results for long-term surface deformation (1994 to 2020). Injection wells are denoted here by small squares. Contours and red color scheme represent the calculated surface deformation measured in meters (m). The locations of east, west, north, and south time series are denoted by black triangles (**Figure 6**).

km<sup>2</sup> surrounding high-rate injectors in the south shows modeled uplift greater than 9 cm. No regions within the study area show any calculated subsidence between 1994 and 2020, which we would expect considering the net-positive change in pore pressure within the injection interval. Subsidence would only be expected if pore pressure dropped below 1994 steady-state levels, which would not occur when only considering injection.

The calculated surface deformation time series for the selected locations (East, West, North, and South) between 1994 and 2020 are shown in **Figure 6**. Deformation first occurred in the western and northeastern region, soon after injection began in 1994. Most of the modeled uplift occurred in the northeast before quickly being overtaken by the eastern and southern in the early 2000s, not long after high-rate injection began in those regions. The spike in surface uplift in the East is followed by an increase in number of magnitude 3.0 and greater earthquakes that includes the August – September 2001 earthquake sequence along the Trinidad fault zone. Between early 2000 and mid-2009, the eastern region experienced the greatest amount of modeled deformation before being overtaken by the southern region, which had the greatest total deformation between 2009 and 2020. The number of earthquakes peaked in 2011 while the south experienced rapid uplift due to injection. The spike in number of earthquakes in 2011 is largely due to the August – September 2011 earthquake sequence along the southern portion of the Trinidad fault zone.

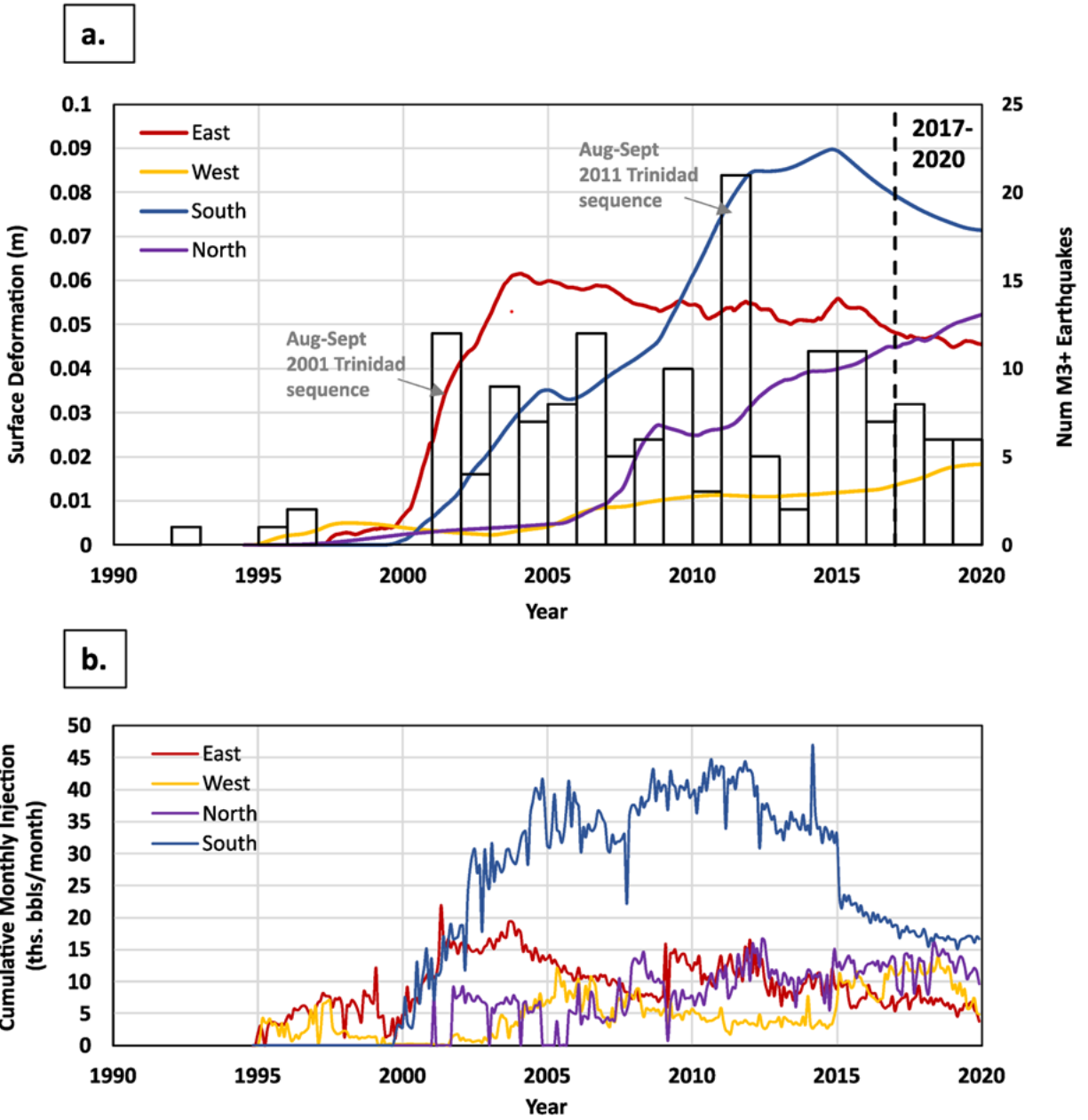


**Figure 6. a.** Colored lines denote surface deformation time series between 1994 and 2020 for the East, West, South, and North time series locations, respectively. The column chart shows magnitude 3.0 and greater earthquakes per year (U.S. Geological Survey ANSS Comprehensive Earthquake Catalog (ComCat), 2023). M 3.0 was previously determined to be the magnitude of completeness between 2000 – 2014 (Rubinstein et al., 2014). Earthquake data shown in **Appendix E**. Deformation time series locations are shown in **Figure 5**. Positive slope indicates uplift while a negative slope indicates subsidence. The regional injection time series is shown in **b.** for reference.

Between 1994 and 2020, the southern region experienced the greatest amount of total modeled uplift. The eastern region had the next greatest total uplift, the north had the third greatest, and the western time series had the smallest magnitude of total modeled uplift, respectively. The deformation is not consistent throughout the duration of the model time. Rather, the modeled deformation at the surface alternates between uplift and subsidence through time, depending on the change of the pore pressure resulting from changes in the rate of fluid injection. When subsidence occurs, it is due to a decrease in injection rate at one or more wells that results in the pore pressure decreasing. The eastern region begins to experience modeled subsidence in late 2003. The southern region experiences the highest rate of modeled subsidence starting in late 2014. The eastern region experiences the most variability between uplift and subsidence over the twenty-six years. The western region experiences some subsidence between 1998 and 2003, but mainly experienced uplift 2003 to 2020. The north experienced mostly calculated uplift.

#### **4.2 Short-term Deformation 2017-2020**

**Figure 7** shows the modeled deformation between 2017 and 2020. This time was chosen to follow a significant decrease in fluid injection rate in the South and highlights how the surface deforms after decreases in pore fluid pressure. Most modeled uplift occurred in the western and northwestern portions of the study area during this time, while areas surrounding injection wells in the south and east experienced subsidence. The maximum modeled uplift was 1.9 cm and the greatest modeled subsidence was roughly 3 cm. The rate and type of deformation between 2017 and 2020 changes over time. Some areas, particularly those within proximity to injection wells, experience both modeled uplift and subsidence through time.

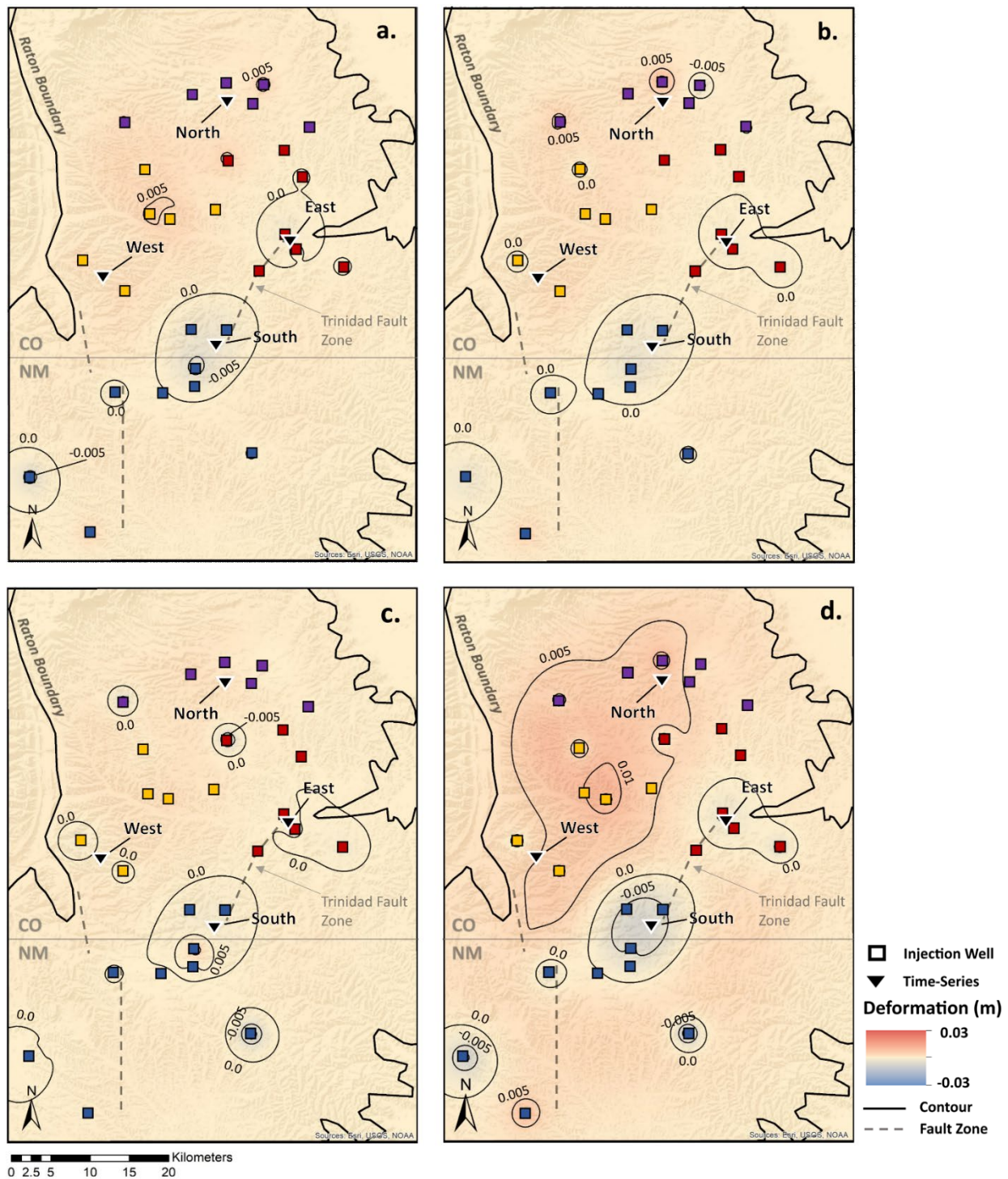


**Figure 7.** Mapped model results for short-term incremental surface deformation. **a.** shows surface deformation between 2017 and 2018, **b.** represents deformation between 2018 and 2019, **c.** shows deformation between 2019 and 2020, and **d.** is total deformation between 2017 and 2020. Injection wells are denoted here by squares colored by region. Contours and blue-red color scheme represent the calculated surface deformation measured in meters (m). The locations of east, west, north, and south time series are denoted by black triangles.

The cumulative volume of wastewater injection does not appear to correspond to modeled deformation. For instance, the southern region surrounding injection wells experienced subsidence despite the overall volume of wastewater injected being larger than other regions that experienced uplift. Subsidence occurs in regions near wells that underwent a decrease in injection rate.

Modeled uplift greater than 5 mm occurs over an area of 517 km<sup>2</sup>, with uplift greater than 1 cm occurs over an area of around 25 km<sup>2</sup>. Modeled subsidence greater than 5 mm occurs over an area of roughly 53 km<sup>2</sup>. Modeled subsidence greater than 1 cm occurs close to injectors at an area of around 2.4 km<sup>2</sup>. The greatest modeled uplift and subsidence occur close to, or directly above, injection wells.

**Figure 6** depicts the time series of surface elevation between 1994 and 2020 for four locations. Deformation between 2017 and 2020 is indicated by the dashed black line. Positive slopes along the curve represent uplift while negative slopes imply subsidence. The eastern region experiences modeled subsidence of about 2.6 mm. Although the East experiences small fluctuations between modeled uplift and subsidence occurring at a frequency less than a year, it overall experiences total subsidence between 2017 and 2020. The West experienced modeled uplift before decreasing in rate, and reaching total uplift of roughly 4.7 mm. The North experienced the greatest amount of modeled uplift between 2017 and 2020 and deformed at the highest rate. It reached a total deformation of close to 7.5 mm. Finally, the South experienced consistent modeled subsidence through the time period, reaching total modeled subsidence of around 8 mm.

## 5. Discussion

### 5.1 Pore Pressure Distribution and Surface Deformation

Varying injection rates through time, and thus fluctuating pore pressures, has implications on the type and rate of calculated deformation over a given time. In the long term (e.g 1994-2020), the greatest modeled surface deformation occurs near the highest-rate injectors. This is unsurprising considering the linear relationship between pressure change and deformation (Brown et al., 2022). However, short-term trends in deformation can deviate from the overall long-term trends.

When fluid is injected into the deep aquifer it increases the pore pressure surrounding the injection site. Over time, the increased pressure diffuses outward from the injection interval. If the injection rate within a region remains high enough to continue to increase the pore pressure surrounding the wells, the area will continue to experience uplift through time. However, if the injection rate decreases sufficiently, the pressure can diffuse quicker than it can be replenished. Subsidence can occur near injection wells when provided there was a sufficient decrease in injection and thus, a decrease in pore pressure.

As such, both the temporal and spatial distribution of calculated surface deformation indicate that the rate of deformation is not constant through time. When observed over the long-term, a point within the study area would show net modeled uplift. However, when observed incrementally, the time-series can show varying rates of both uplift and subsidence. The East time-series provides a good example of this phenomenon (**Figure 6**). The rate of

surface deformation fluctuates between subsidence and uplift through time, which would otherwise be overlooked when only considering long-term results.

Total volume injected over time and monthly injection rate can be good indicators of where deformation occurs within the Raton Basin in the long term. For instance, the greatest injection volume (along with the highest monthly injection rate) occurs surrounding several of the southern injection wells in New Mexico. As a result, this region experienced the greatest amount of total calculated uplift between 1994 and 2020. However, the rate of injection and total volume does not appear to be a good indicator of the type, distribution, and magnitude of deformation when observed in the short term. Between 2017 and 2020, a decrease in surface elevation is calculated surrounding the highest rate injectors in the South.

## **5.2 Surface Deformation and Earthquake Occurrence**

Rubinstein et al. (2014) determined a magnitude of completeness for earthquakes in the Raton Basin between 2001-2014 of M 3.0. Starting with the 2001 Trinidad earthquake sequence, there has been a striking increase in the number of magnitude 3.0 or greater earthquakes in the following years. The number of earthquakes peaked during the 2011 earthquake sequence in the southern portion of the Trinidad fault zone. The largest magnitude recorded earthquake in Raton Basin history occurred during this time. Both notable earthquake sequences coincide with modeled rapid uplifting episodes. As shown in **Figure 6**, the 2001 Trinidad sequence follows the onset of modeled rapid uplift in the East. The 2011 sequence occurs during the rapid uplifting in the South. The greatest total calculated uplift occurred in the South as well as the greatest number of earthquake occurrences in 2011s. The overall

number of yearly magnitude 3 and greater earthquake occurrences increases after the surface elevation increases throughout the Basin. The timing of increased earthquake occurrences and notable seismic sequence events with calculated surface uplift suggests correlation between the two phenomena.

### **5.3 Why is there subsidence in the South and East?**

Previous studies dealing with Class II wastewater injection and surface deformation have noted subsidence occurring near injection wells, many of which are high-rate injectors. Deng et al. (2019) observed both uplift and subsidence occurring near injection wells in Texas. They suggest that subsidence may be related to groundwater withdrawal. Using InSAR data, Barnhart et al. (2014) found regions of subsidence within the Raton basin at different times between 1999 to 2011. Though various mechanisms can create subsidence observed at the surface, it was previously unknown as to what impact fluid injection had on causing the subsidence.

Our results suggest that fluid injection can play a role in creating subsidence observable at the land surface due to a “deflation” effect after a decrease in injection rate. This is especially true when observed in short term, incremental steps. The rate of injection does not appear to be a factor in determining where modeled subsidence occurs. Rather, it is the significant decrease in monthly injection rate that created subsidence. The southern and eastern portions of the Raton Basin provide a good example of this phenomenon as shown in **Figure 8**.

The South experienced the highest rate of injection between 2017 and 2020 and had consistently the highest rate of injection since early 2001. This would imply that the injection

interval in the South experiences the greatest overall increase in pore pressure since injection began. Consequentially, the southern part of the Raton basin experiences the most total calculated uplift between 1994 and 2020. However, the modeled incremental deformation

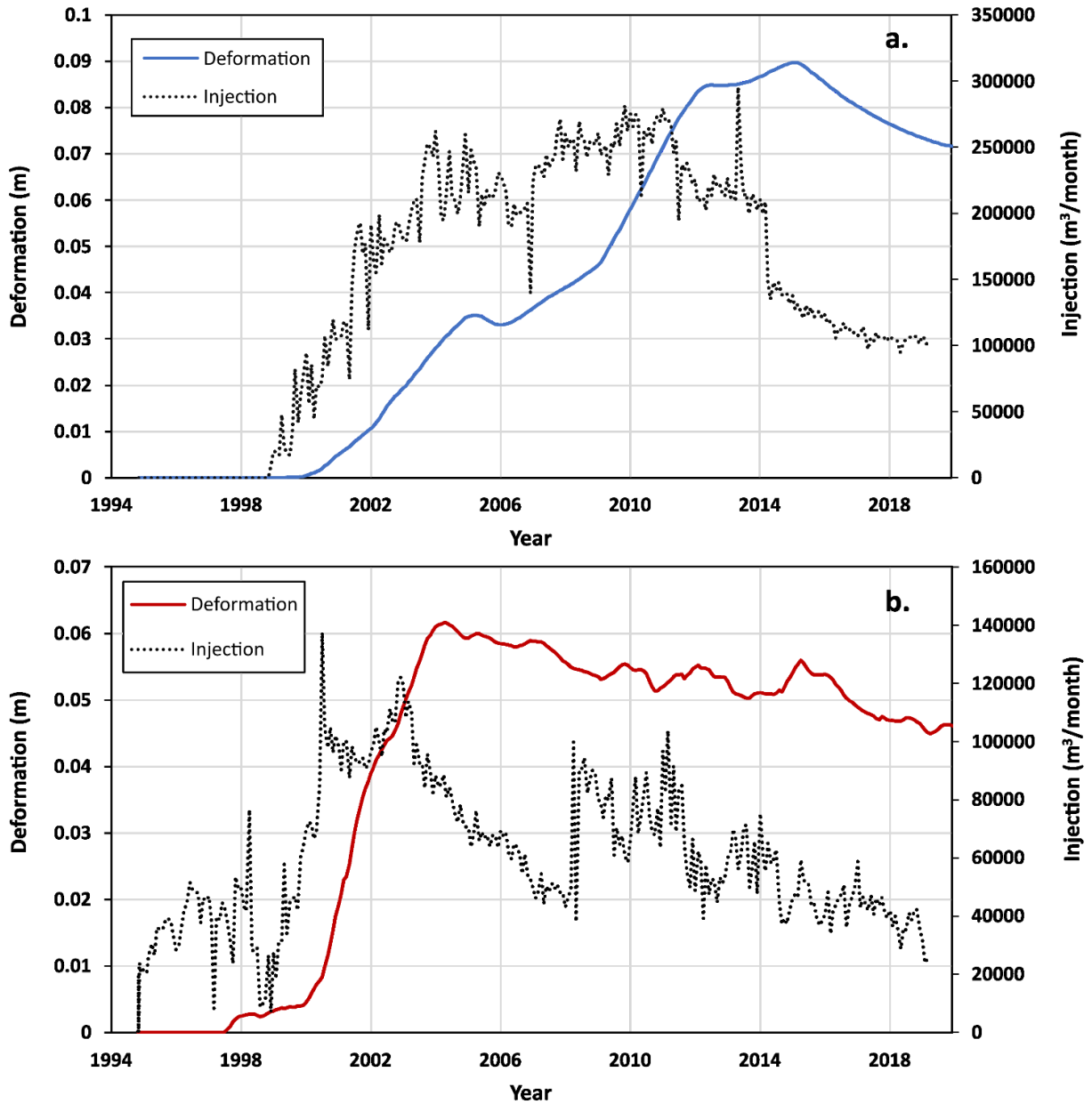


**Figure 8:** Comparison between modeled surfaced deformation at time series location and its respective regional wastewater injection rate. **a.** shows the injection and deformation timeseries in the southern portion of the study area, and **b.** represents deformation and injection in the eastern portion of the study area. Subsidence in both regions occurs soon after an overall decrease in total regional injection rate.

between 2017 and 2020 shows subsidence surrounding several of the high-rate injectors in New Mexico. The eastern region had the lowest injection rate by 2020 but had the 2<sup>nd</sup> highest to highest injection rate early in the region's history. The decrease in injection rate appears to have resulted in modeled subsidence.

By comparing the total regional injection rate for the southern and eastern wells along with their corresponding modeled surface deformation, we suggest that the subsidence occurs soon after a significant decrease in the monthly regional rate of injection (**Figure 8**). The decrease in monthly injection rate results in a decrease in pore pressure in both regions. This implies that the rate of pressure diffusion exceeded the injection wells' ability to increase the pore pressure in the aquifer, leading to pore pressure decreasing. There is some lag time between when the injection rate declines and when the surface begins to subside. The relation between pressure change and surface deformation is assumed to be instantaneous (Brown et al. 2022), so any lag time between the decrease in injection rate and subsidence is primarily due to the rate of pressure diffusion.

#### **5.4 Additional Mechanisms Impacting Surface Deformation**

Surface deformation is likely a result of multiple processes and our model focuses on only the contribution of surface deformation resulting from wastewater injection. For instance, numerous other anthropogenic activities can cause deformation such as mining, oil and gas production, or groundwater extraction (e.g. Galloway & Hoffmann, 2007; Deng et al., 2020; Bagheri-Gavkosh et al., 2021). Our model also does not account for other natural deforming phenomena such as aseismic creep (Tiampo et al. 2013) and earthquake slip (Atzori et al., 2009,

Barnhart et al. 2014). Furthermore, surface deformation can also be related to surficial erosional or depositional activity. The rate and magnitude of surface deformation due to these mechanisms remains uncertain.

It is possible oil and gas production activities can impact surface deformation through mechanisms other than fluid injection. There is an abundance of production wells operating within the Raton Basin (COGCC, 2020; NMOCD, 2020). Previous studies have observed a poroelastic response to extraction within oil and gas producing regions (e.g., Deng et al., 2020). We note that, surface deformation due to oil and gas production can be considered negligible if the production is primarily through enhanced oil recovery where injected fluid volume is nearly equal the extracted volume of fluid (Rubinstein and Mahani 2015; Brown et al, 2022).

Groundwater depletion has been shown to result in uplift related to lithospheric rebound in some areas (Holzer et al., 1979; Amos et al., 2014; Borsa et al., 2014, White et al., 2022). When large volumes of fluid are extracted from aquifers, the overall crustal mass decreases resulting in the unloading of the lithosphere. A study by Amos et al. (2014) used GPS measurements of vertical surface displacements to show that a substantial region of rock uplift up to 1-3 mm/year surrounding the southern San Joaquin Valley of California that has experienced significant groundwater extraction for agricultural use. Water has been extracted from the Raton Basin during coalbed methane and gas production since 1990s, with the water production rate reaching a rate of over 140 million barrels a year in some years. However, first order estimates of lithospheric rebound due to the water extraction suggest negligible uplift **(Appendix B)**.

## 6. Conclusion

This study calculates surface deformation due to injection induced pressure perturbations in the long-term (1994-2020) and in short-term, incremental steps (2017-2020). Time-series of deformation in four locations show how deformation may respond to changing fluid injection rates. From our model results, we draw the following conclusions:

1. In the long-term, the entire study area saw a calculated increase in surface elevation. The greatest modeled uplift occurred in the South where most of the wastewater was injected.
2. Thus, in the long-term, the magnitude and the areal extent of uplift is controlled by cumulative injection volume.
3. Seismicity follows periods of calculated uplifting. Increased seismicity and the timing of notable seismic sequence events along the Trinidad fault zone correspond to modeled uplifting events due to injection. Surface deformation is related to the same pressure perturbations caused by fluid injection that can initiate seismicity.
4. Substantial decreases in injection rate can result in a sufficient decline in aquifer pore pressure resulting in modeled short-term subsidence at the surface.
5. Therefore, short-term deformation due to injection is controlled by increases and decreases in the rate of injection opposed to total volume of fluid injected. Past decreases in injection rates explain the modeled subsidence between 2017-2020 in the South and East, despite the south seeing the highest total injection.

6. The land surface surrounding injection wells does not necessarily continue to uplift while wastewater is injected. Rather, surface deformation due to injection fluctuates between uplift and subsidence through time following increases and decreases in injection rate.

## References

- Amos, C. B., Audet, P., Hammond, W. C., Bürgmann, R., Johanson, I. A., & Blewitt, G. (2014). Uplift and seismicity driven by groundwater depletion in central California. *Nature*, 509(7501), 483–486. <https://doi.org/10.1038/nature13275>
- Atzori, S., Hunstad, I., Chini, M., Salvi, S., Tolomei, C., Bignami, C., Stramondo, S., Trasatti, E., Antonioli, A., & Boschi, E. (2009). Finite fault inversion of DInSAR coseismic displacement of the 2009 L'Aquila earthquake (central Italy): THE 2009 L'AQUILA EARTHQUAKE BY DINSAR. *Geophysical Research Letters*, 36(15), n/a-n/a. <https://doi.org/10.1029/2009GL039293>
- Bagheri-Gavkosh, M., Hosseini, S. M., Ataie-Ashtiani, B., Sohani, Y., Ebrahimian, H., Morovat, F., & Ashrafi, S. (2021). Land subsidence: A global challenge. *Science of The Total Environment*, 778, 146193. <https://doi.org/10.1016/j.scitotenv.2021.146193>
- Baltz, E. H. (1965). Stratigraphy and history of Raton basin and notes on San Luis basin, Colorado-New Mexico. *AAPG Bulletin*, 49(11), 2041-2075. <https://doi-org.colorado.idm.oclc.org/10.1306/a6633882-16c0-11d7-8645000102c1865d>
- Barba-Sevilla, M., Baird, B., Liel, A., & Tiampo, K. (2018). Hazard Implications of the 2016 Mw 5.0 Cushing, OK Earthquake from a Joint Analysis of Damage and InSAR Data. *Remote Sensing*, 10(11), 1715. <https://doi.org/10.3390/rs10111715>
- Barnhart, W. D., Benz, H. M., Hayes, G. P., Rubinstein, J. L., & Bergman, E. (2014). Seismological and geodetic constraints on the 2011 Mw5. 3 Trinidad, Colorado earthquake and induced deformation in the Raton Basin. *Journal of Geophysical Research: Solid Earth*, 119(10), 7923-7933. <http://doi.wiley.com/10.1002/2014JB011227>
- Borsa, A. A., Agnew, D. C., & Cayan, D. R. (2014). Ongoing drought-induced uplift in the western United States. *Science*, 345(6204), 1587–1590. <https://doi.org/10.1126/science.1260279>
- Brown, M. R., Ge, S., & Sreaton, E. (2022). A Simple Relation to Constrain Groundwater Models Using Surface Deformation. *Groundwater*, 60(3), 410-417. <https://doi.org/10.1111/gwat.13148>
- Brown, M. R. M., Ge, S., Sheehan, A. F., & Nakai, J. S. (2017). Evaluating the effectiveness of induced seismicity mitigation: Numerical modeling of wastewater injection near Greeley, Colorado. *Journal of Geophysical Research: Solid Earth*, 122(8), 6569–6582. <https://doi.org/10.1002/2017JB014456>

- Chang, K. W., & Segall, P. (2016). Injection-induced seismicity on basement faults including poroelastic stressing. *Journal of Geophysical Research: Solid Earth*, 121(4), 2708-2726. <https://doi.org/10.1002/2015JB012561>
- Clark, J. E., Bonura, D. K., & Van Voorhees, R. F. (2005). An overview of injection well history in the United States of America. *Developments in water science*, 52, 3-12. [https://doi.org/10.1016/S0167-5648\(05\)52001-X](https://doi.org/10.1016/S0167-5648(05)52001-X)
- Colorado Oil and Gas Conservation Commission (2020). Colorado Oil and Gas Conservation Commission, COGCC website. [Retrieved from [http://cogcc.state.co.us/data.html#/cogis.](http://cogcc.state.co.us/data.html#/cogis)] (Accessed 20 July 2020)
- Davis, S.D., and C. Frohlich (1993), Did (or will) fluid injection cause earthquakes? – Criteria for a rational assessment, *Seismological Research Letters*, 64(3-4), 207-224. <https://doi.org/10.1785/gssrl.64.3-4.207>
- Deng, F., Dixon, T. H., & Xie, S. (2020). Surface Deformation and Induced Seismicity Due to Fluid Injection and Oil and Gas Extraction in Western Texas. *Journal of Geophysical Research: Solid Earth*, 125(5). <https://doi.org/10.1029/2019JB018962>
- Detournay, E., & Cheng, A. H.-D. (1993). Fundamentals of Poroelasticity. In *Analysis and Design Methods* (pp. 113–171). Elsevier. <https://doi.org/10.1016/B978-0-08-040615-2.50011-3>
- Ellsworth, W. L. (2013). Injection-Induced Earthquakes. *Science*, 341(6142), 1225942. <https://doi.org/10.1126/science.1225942>
- Fetter, C. W. (2018). *Applied hydrogeology*. Waveland Press.
- Freeze, R.A., & J.A. Cherry. (1979). *Groundwater*. Prentice-Hall, Inc.
- Gabriel, A. K., Goldstein, R. M., & Zebker, H. A. (1989). Mapping small elevation changes over large areas: Differential radar interferometry. *Journal of Geophysical Research: Solid Earth*, 94(B7), 9183-9191. <https://doi.org/10.1029/JB094iB07p09183>
- Galloway, D. L., & Hoffmann, J. (2007). The application of satellite differential SAR interferometry-derived ground displacements in hydrogeology. *Hydrogeology Journal*, 15(1), 133–154. <https://doi.org/10.1007/s10040-006-0121-5>
- Ge, S., & Gorelick, S. M. (2015). Hydrology, Floods and Droughts. *Groundwater and Surface Water. Reference Module in Earth Systems and Environmental Sciences*, from *Encyclopedia of Atmospheric Sciences*,, 209-216.

- Ge, S., & Saar, M. O. (2022). Review: Induced Seismicity During Geoenergy Development—A Hydromechanical Perspective. *Journal of Geophysical Research: Solid Earth*, 127(3). <https://doi.org/10.1029/2021JB023141>
- Goebel, T. H. W., Weingarten, M., Chen, X., Haffener, J., & Brodsky, E. E. (2017). The 2016 Mw5.1 Fairview, Oklahoma earthquakes: Evidence for long-range poroelastic triggering at >40 km from fluid disposal wells. *Earth and Planetary Science Letters*, 472, 50–61. <https://doi.org/10.1016/j.epsl.2017.05.011>
- Harbaugh, A. W., Banta, E. R., Hill, M. C., & Macdonald, M. G. (2005). The US geological survey modular ground water models: User guide to modulization concepts and the groundwater flow process. *US Geological Survey*, 121.
- Healy, J. H., Rubey, W. W., Griggs, D. T., & Raleigh, C. B. (1968). The Denver earthquakes. *Science*, 161(3848), 1301-1310. [https://doi.org-colorado.idm.oclc.org/10.1126/science.161.3848.1301](https://doi.org/colorado.idm.oclc.org/10.1126/science.161.3848.1301)
- Holzer, T. L. (1979). Elastic expansion of the lithosphere caused by groundwater depletion. *Journal of Geophysical Research*, 84(B9), 4689. <https://doi.org/10.1029/JB084iB09p04689>
- Hornbach, M. J., DeShon, H. R., Ellsworth, W. L., Stump, B. W., Hayward, C., Frohlich, C., Oldham, H. R., Olson, J. E., Magnani, M. B., Brokaw, C., & Luetgert, J. H. (2015). Causal factors for seismicity near Azle, Texas. *Nature Communications*, 6(1), 6728. <https://doi.org/10.1038/ncomms7728>
- Horton, S. (2012). Disposal of Hydrofracking Waste Fluid by Injection into Subsurface Aquifers Triggers Earthquake Swarm in Central Arkansas with Potential for Damaging Earthquake. *Seismological Research Letters*, 83(2), 250–260. <https://doi.org/10.1785/gssrl.83.2.250>
- Hubbert, M. K., & Rubey, W. W. (1959). Role of fluid pressure in mechanics of overthrust faulting: I. Mechanics of fluid-filled porous solids and its application to overthrust faulting. *Geological Society of America Bulletin*, 70(2), 115-166. [https://doi-org.colorado.idm.oclc.org/10.1130/0016-7606\(1961\)72%5B1445:ROFPIM%5D2.0.CO;2](https://doi.org/colorado.idm.oclc.org/10.1130/0016-7606(1961)72%5B1445:ROFPIM%5D2.0.CO;2)
- Keranen, K. M., Weingarten, M., Abers, G. A., Bekins, B. A., & Ge, S. (2014). Sharp increase in central Oklahoma seismicity since 2008 induced by massive wastewater injection. *Science*, 345(6195), 448–451. <https://doi.org/10.1126/science.1255802>
- Jiang, Y., Dixon, T. & Wdowinski, S. Accelerating uplift in the North Atlantic region as an indicator of ice loss. *Nature Geosci* 3, 404–407 (2010). <https://doi.org/10.1038/ngeo845>

- Kim, J.-W., & Lu, Z. (2018). Association between localized geohazards in West Texas and human activities, recognized by Sentinel-1A/B satellite radar imagery. *Scientific Reports*, 8(1), 4727. <https://doi.org/10.1038/s41598-018-23143-6>
- Kuang, X., and Jiao, J. J. (2014), An integrated permeability-depth model for Earth's crust, *Geophys. Res. Lett.*, 41, 7539– 7545, doi:10.1002/2014GL061999.
- Kuang, X., Jiao, J. J., Zheng, C., Cherry, J. A., & Li, H. (2020). A review of specific storage in aquifers. *Journal of Hydrology*, 581, 124383. <https://doi-org.colorado.idm.oclc.org/10.1016/j.jhydrol.2019.124383>
- Lanari, R., Casu, F., Manzo, M., Zeni, G., Berardino, P., Manunta, M., & Pepe, A. (2007). An overview of the small baseline subset algorithm: A DInSAR technique for surface deformation analysis. *Deformation and Gravity Change: Indicators of Isostasy, Tectonics, Volcanism, and Climate Change*, 637-661.
- Loesch, E., & Sagan, V. (2018). SBAS Analysis of Induced Ground Surface Deformation from Wastewater Injection in East Central Oklahoma, USA. *Remote Sensing*, 10(2), 283. <https://doi.org/10.3390/rs10020283>
- Massonnet, D., and Feigl, K. L. (1998), Radar interferometry and its application to changes in the Earth's surface, *Rev. Geophys.*, 36( 4), 441– 500, doi:10.1029/97RG03139.
- Menezes, E. A. (2022). Geodetic techniques applied towards understanding induced seismicity in raton basin, colorado & new mexico (Order No. 29398395). Available from Dissertations & Theses @ University of Colorado, Boulder; Dissertations & Theses @ University of Colorado System. (2765096955). Retrieved from <https://colorado.idm.oclc.org/login?url=https://www.proquest.com/dissertations-theses/geodetic-techniques-applied-towards-understanding/docview/2765096955/se-2>
- Nakai, J. S., Weingarten, M., Sheehan, A. F., Bilek, S. L., & Ge, S. (2017). A possible causative mechanism of Raton Basin, New Mexico and Colorado earthquakes using recent seismicity patterns and pore pressure modeling. *Journal of Geophysical Research: Solid Earth*, 122, 8051– 8065. <https://doi.org/10.1002/2017JB014415>
- New Mexico Oil Conservation Division. (2020). New Mexico Oil and Conservation Division, 2016, permitting. [Retrieved from <https://wwwapps.emnrd.state.nm.us/ocd/ocdpermitting/data/wells.aspx>] (Accessed 20 July 2020)
- Notti, D., Calò, F., Cigna, F., Manunta, M., Herrera, G., Berti, M., ... & Zucca, F. (2015). A user-oriented methodology for DInSAR time series analysis and interpretation: Landslides and

- subsidence case studies. *Pure and Applied Geophysics*, 172(11), 3081-3105.  
<https://doi.org/10.1007/s00024-015-1071-4>
- Peltzer, G., & Rosen, P. (1995). Surface displacement of the 17 May 1993 Eureka Valley, California, earthquake observed by SAR interferometry. *Science*, 268(5215), 1333-1336.  
<https://doi-org.colorado.idm.oclc.org/10.1126/science.268.5215.1333>
- Poland, J. F., & Davis, G. H. (1969). Land subsidence due to withdrawal of fluids. <https://doi-org.colorado.idm.oclc.org/10.1130/REG2-p187>
- Reasenber, P. A., & Simpson, R. W. (1992). Response of Regional Seismicity to the Static Stress Change Produced by the Loma Prieta Earthquake. *Science*, 255(5052), 1687–1690.  
<https://doi.org/10.1126/science.255.5052.1687>
- Rosen, P. A., Hensley, S., Joughin, I. R., Li, F. K., Madsen, S. N., Rodriguez, E., & Goldstein, R. M. (2000). Synthetic aperture radar interferometry. *Proceedings of the IEEE*, 88(3), 333-382. doi: 10.1109/5.838084
- Rubinstein, J. L., Ellsworth, W. L., McGarr, A., & Benz, H. M. (2014). The 2001-Present Induced Earthquake Sequence in the Raton Basin of Northern New Mexico and Southern Colorado. *Bulletin of the Seismological Society of America*, 104(5), 2162–2181.  
<https://doi.org/10.1785/0120140009>
- Rubinstein, J. L., & Mahani, A. B. (2015). Myths and Facts on Wastewater Injection, Hydraulic Fracturing, Enhanced Oil Recovery, and Induced Seismicity. *Seismological Research Letters*, 86(4), 1060–1067. <https://doi.org/10.1785/0220150067>
- Schindler, S., Hegemann, F., Koch, C., König, M., & Mark, P. (2016). Radar interferometry based settlement monitoring in tunnelling: Visualisation and accuracy analyses. *Visualization in Engineering*, 4(1), 7. <https://doi.org/10.1186/s40327-016-0034-x>
- Schmidt, D. A., & Bürgmann, R. (2003). Time-dependent land uplift and subsidence in the Santa Clara valley, California, from a large interferometric synthetic aperture radar data set. *Journal of Geophysical Research: Solid Earth*, 108(B9). <https://doi-org.colorado.idm.oclc.org/10.1029/2002JB002267>
- Shirzaei, M., Ellsworth, W. L., Tiampo, K. F., Gonzalez, P. J., & Manga, M. (2016). Surface uplift and time-dependent seismic hazard due to fluid injection in eastern Texas. *Science*, 353(6306), 1416–1419. <https://doi.org/10.1126/science.aag0262>
- Shirzaei, M., Manga, M., & Zhai, G. (2019). Hydraulic properties of injection formations constrained by surface deformation. *Earth and Planetary Science Letters*, 515, 125–134. <https://doi.org/10.1016/j.epsl.2019.03.025>

- Stein, R. S. (1999). The role of stress transfer in earthquake occurrence. *Nature*, 402(6762), 605–609. <https://doi.org/10.1038/45144>
- Stokes, S. M., Ge, S., Brown, M. R. M., Menezes, E. A., Sheehan, A. F., & Tiampo, K. F. (2023). Pore pressure diffusion and onset of induced seismicity. *Journal of Geophysical Research: Solid Earth*, 128, e2022JB026012. <https://doi-org.colorado.idm.oclc.org/10.1029/2022JB026012>
- Teatini, P., Gambolati, G., Ferronato, M., Settari, A. (Tony), & Walters, D. (2011). Land uplift due to subsurface fluid injection. *Journal of Geodynamics*, 51(1), 1–16. <https://doi.org/10.1016/j.jog.2010.06.001>
- Terzaghi, K. (1925). *Erdbaumechanik auf bodenphysikalischer Grundlage*. F. Deuticke.
- Tiampo, K. F., González, P. J., & Samsonov, S. S. (2013). Results for aseismic creep on the Hayward fault using polarization persistent scatterer InSAR. *Earth and Planetary Science Letters*, 367, 157–165. <https://doi.org/10.1016/j.epsl.2013.02.019>
- U.S. Geological Survey (2023). U.S. Geological Survey ANSS Comprehensive Earthquake Catalog (ComCat). [Retrieved from <https://earthquake.usgs.gov/earthquakes/search/>] (Accessed 19 February 2023)
- Wang, H. F. (2000). *Theory of linear poroelasticity with applications to geomechanics and hydrogeology* (Vol. 2). Princeton university press.
- Weingarten, M. B. (2015). On the interaction between fluids and earthquakes in both natural and induced seismicity (Order No. 3743635). Available from Dissertations & Theses @ University of Colorado, Boulder; Dissertations & Theses @ University of Colorado System; ProQuest Dissertations & Theses A&I. (1752515717). Retrieved from <https://colorado.idm.oclc.org/login>
- Weingarten, M., S. Ge, J. W. Godt, B. A. Bekins, and J. L. Rubinstein (2015), High-rate injection is associated with the increase in U.S. mid-continent seismicity, *Science*, 348(6241), 1336–1340, doi:10.1126/science.aab1345
- White, A. M., Gardner, W. P., Borsa, A. A., Argus, D. F., & Martens, H. R. (2022). A Review of GNSS/GPS in Hydrogeodesy: Hydrologic Loading Applications and Their Implications for Water Resource Research. *Water Resources Research*, 58(7). <https://doi.org/10.1029/2022WR032078>
- Zebker, H. A., & Villasenor, J. (1992). Decorrelation in interferometric radar echoes. *IEEE Transactions on geoscience and remote sensing*, 30(5), 950-959.

Zhang, Y., Person, M., Rupp, J., Ellett, K., Celia, M.A., Gable, C.W., Bowen, B., Evans, J., Bandilla, K., Mozley, P., Dewers, T. and Elliot, T. (2013), Hydrogeologic Controls on Induced Seismicity in Crystalline Basement Rocks Due to Fluid Injection into Basal Reservoirs. *Groundwater*, 51: 525-538. <https://doi.org/10.1111/gwat.12071>

## Appendix A: Detailed Modelling Methodology

### A.1. Injection Well Data

For this study, we use a three-dimensional basin-scale groundwater flow model of the Raton Basin developed by Stokes et al. (2023). For this study, we made only very minor alterations in parameters used and the discretization. Here, we briefly summarize the methods used to model pore pressure diffusion. For a more detailed description, refer to Stokes et al. (2023).

An integral first step in this project was the aggregation of injection data and information regarding well construction. Monthly injection rates, along with well coordinates, screening interval depths, and start dates for the Class II injection wells in Colorado and New Mexico were retrieved from the Colorado Oil and Gas Commission (COGCC, 2020) and the New Mexico Oil Conservation Division (NMOCD, 2020), respectively (Stokes et al., 2023). Wastewater injection began in Colorado in 1994 (COGCC, 2020). Wastewater injection began in New Mexico in 1999, but injection rates were not recorded prior to May 2006 (NMOCD, 2020). The rate of production in New Mexico, however, was reported during this time. Previous studies have used production data to estimate unreported wastewater injection rates (Rubinstein et al., 2014; Nakai et al., 2017). The assumption is that the volume of injected water is roughly equal to the volume of fluids produced. To account for the missing data, the production rates between 1999 and 2006 were used to estimate injection rates during this time (Stokes et al, 2023).

To better understand the relation between the rate of injection and regional deformation, the study area was subdivided into four regions: East, West, North, and South. The twenty-nine injection wells were categorized based on the subregion.

## **A.2. Pore Pressure Modeling**

The model was ran using MODFLOW-2005, a commonly used Fortran code package developed by the USGS (Harbaugh et al., 2005). The modeling package is designed to simulate the change in hydraulic head distribution over time in a groundwater system due to pressure perturbations such as pumping and injection. The code numerically calculates head change at select time steps using the groundwater flow equation (equation 1 in an earlier section).

The model domain has dimensions of 130km x 200 km x 11-14km (depth) and was discretized into approximately 5.5 million cells. Within the study area, the cells have dimensions of 250m x 250m, while the cells outside the study area are larger; 1km x 1km. Top elevations of the modeled hydrostratigraphic units (upper aquifer, middle injection zone, and basement) were interpolated using data from well lithology logs and Precambrian basement data (Stokes et al., 2023). Each hydrogeologic unit is vertically discretized into 38 total layers; 6 layers in the upper/aquifer, 12 layers in the middle aquifer, and 20 layers in the basement. A simplified example is shown in **Figure A-1**.

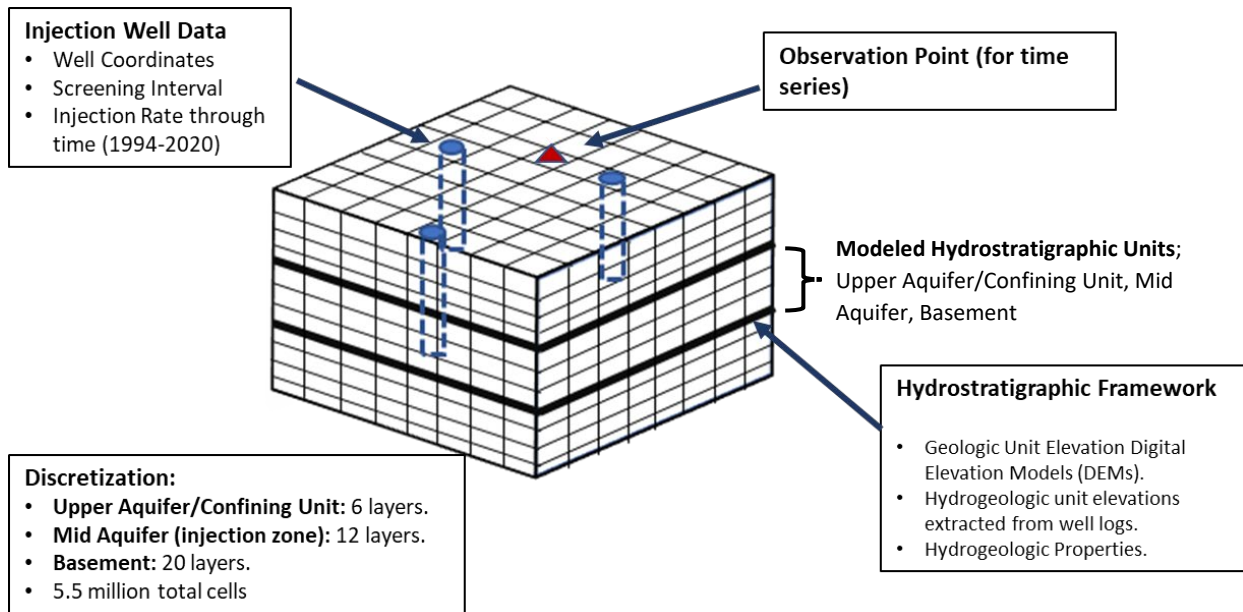


**Figure A-1:** Diagram depicting generalized MODFLOW-2005 model development methodology and input data. A model domain representing the basin hydrostratigraphy was built using digital elevation models (DEMs) of the surface, geological unit elevations gathered from well lithology logs and geologic maps, and Precambrian basement data found in literature (Stokes et al., 2023). Each modeled layer was assigned respective hydrogeologic properties ( e.g. hydraulic conductivity ( $K$ ), specific storage  $S_s$ ). The model was discretized into of 5.5 million total cells. Injection well data, including injection rate through time and screening interval depth is inputted into the model domain. Finally, for this study, we included observation points to represent where uplift time series are calculated.

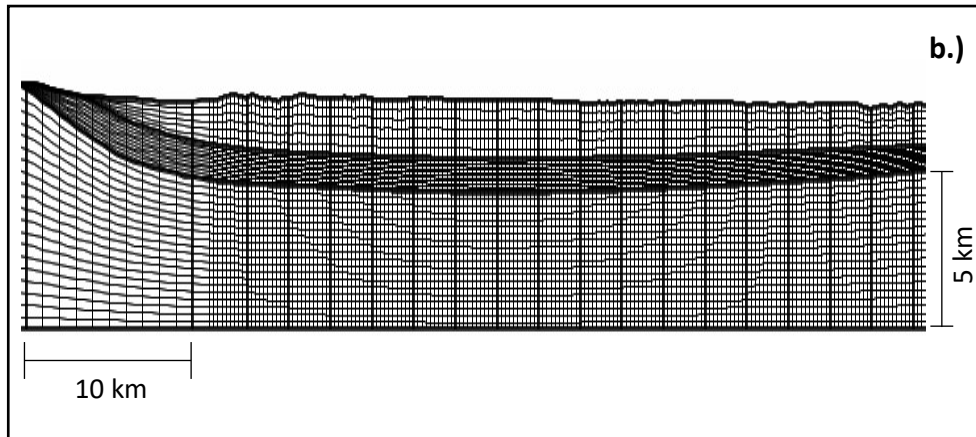
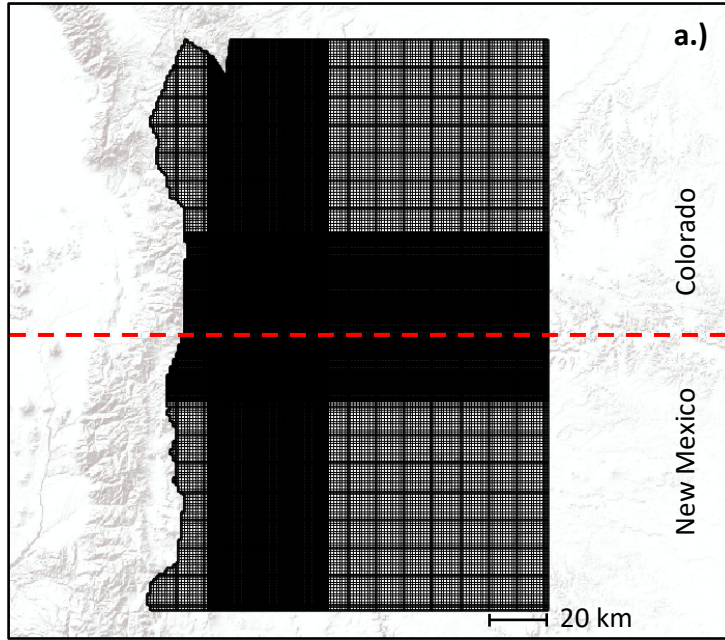


**Figure A-2:** Pore Pressure Model Domain. **a.** shows the entire model domain in aerial view (from Stokes et al. 2023). **b.** represents the finely discretized portion of the model domain in cross-sectional view.

Each model layer was assigned the hydrogeologic parameters necessary to compute pressure change (**Table A-1**). Hydraulic conductivity ( $K$ ) refers to the rate at which water can flow within a permeable medium (Fetter, 2018). Specific storage ( $S_s$ ) describes the volume of water that can be released from, or stored in, a unit volume of aquifer per unit change in head (Freeze and Cherry, 1979; Fetter 2018; Kuang et al, 2020). The parameter, hydraulic diffusivity ( $\omega$ ), describes the ability of fluid pressure to diffuse within a saturated porous medium and is a function of both the medium and fluid properties (Freeze & Cherry, 1979). While conventionally written with the letter “ $D$ ”, we write diffusivity as  $\omega$  because  $D$  refers to surface deformation in this research. It can be derived from the ratio of hydraulic conductivity to specific storage (equation 4).

$$\omega = \frac{K}{S_s} \quad (4)$$

where  $\omega$  is diffusivity ( $L^2T^{-1}$ ),  $K$  is hydraulic conductivity ( $L T^{-1}$ ) and  $S_s$  is specific storage ( $L^{-1}$ ).

When considering both pressure and temperature gradients, the equation becomes

$$\omega = \frac{k}{\mu(\alpha + n\beta)} \quad (5)$$

where  $k$  is permeability ( $L^2$ ),  $n$  is porosity (1),  $\mu$  is dynamic viscosity ( $L T^{-1} M^{-1}$ ),  $\alpha$  is rock compressibility, and  $\beta$  is fluid compressibility ( $L T^2M^{-1}$ ).

Model parameters used in this study were gathered from literature values of hydrogeologic properties from within the Raton Basin and proxy locations (Stokes et al., 2023).

The basement diffusivity was determined using the depth decaying permeability function (equation 6) from Kuang and Jiao (2014):

$$\log k = \log k_r + (\log k_s - \log k_r)(1 + z)^{-\alpha} \quad (6)$$

where  $k$  is permeability ( $L^2$ ),  $k_s$  is the permeability when depth is equal to zero ( $L^2$ ),  $k_r$  is the residual permeability at depth ( $L^2$ ),  $z$  is the depth in kilometers ( $L$ ) and  $\alpha$  is the decay index (1).

The hydrogeologic parameters used in this study are shown in **Table A-1**.

**Table A-1: Hydrogeologic parameters used in study.**

Hydrostratigraphic Units	Hydraulic Conductivity (m/s)	Specific Storage ( $m^{-1}$ )	Diffusivity ( $m^2/s$ )
Hydraulic Barrier	$\sim 1.0 \times 10^{-14}$	$10^{-5}$	$\sim 10^{-9}$
Injection Interval	$10^{-7}$	$10^{-5}, 10^{-6}, 10^{-7}$	0.1, 1.0, 10
Precambrian Basement	Depth decaying	$10^{-7}$	Depth decaying

Well data, including monthly injection rates, screening interval elevations, and location coordinates were retrieved from COGCC (2020) and NMOCD (2020) and used as model inputs. Fluid injection creates perturbations within the pore pressure regime in the aquifer through time which is simulated using the groundwater flow model. For this study, we are interested in looking at total surface deformation between 1994 and 2020, and incremental deformation

between 2017 and 2020. We calculate surface deformation due to pressure changes using the calculated hydraulic head ( $h$ ) distribution at various time steps.

Hydraulic head ( $h$ ) is a fundamental parameter in hydrogeology describing the mechanical energy per unit weight of water within an aquifer and has dimensions of length (L). It is the sum of elevation head ( $h_z$ ) and pressure head ( $h_p$ ):

$$h = h_z + h_p \quad (7)$$

Elevation head  $h_z$  (L) is measured as the height of the fluid above a specified datum, representing gravitational potential energy. Pressure head  $h_p$  (L) describes the mechanical energy due to pore fluid pressure. It is written as the ratio of pore pressure over the product of fluid density and gravitational acceleration.

$$h_p = \frac{p}{\rho g} \quad (8)$$

where  $p$  is pore fluid pressure ( $M L^{-1}T^{-2}$ ),  $\rho$  is fluid density ( $ML^{-3}$ ), and  $g$  is gravitational acceleration ( $L T^{-2}$ ). We assume that the elevation head, density of water, and gravitational acceleration remain constant. Therefore, the change in hydraulic head  $h$  is directly proportional to the change in pore fluid pressure due to wastewater injection. The model began with an initial hydraulic head of 5000 meters in every cell within the discretized domain, representing steady-state conditions (Stokes et al., 2023). Deviations from the initial head over time are due to pore fluid pressure changes related to wastewater injection.

After simulating hydraulic change due to wastewater injection between 1994 and 2020, hydraulic head distribution results between 1994 and 2020, 2017 and 2018, 2018 and 2019, and 2019 and 2020, respectively, were extracted for each discretized model layer. The difference in head between the respective time steps was used to calculate the change in head ( $\Delta h$ ). **Figure A-3** represents the pressure distribution results for layer 8 of the model (within the injection layer) for years 2017 and 2020 as an example of a piece of the data used (all layers were incorporated). For each specified time-series location, we used the open-source software package GW\_Chart to extract time series of hydraulic head (h) change between 1994 and 2020 within each discretized model layer.

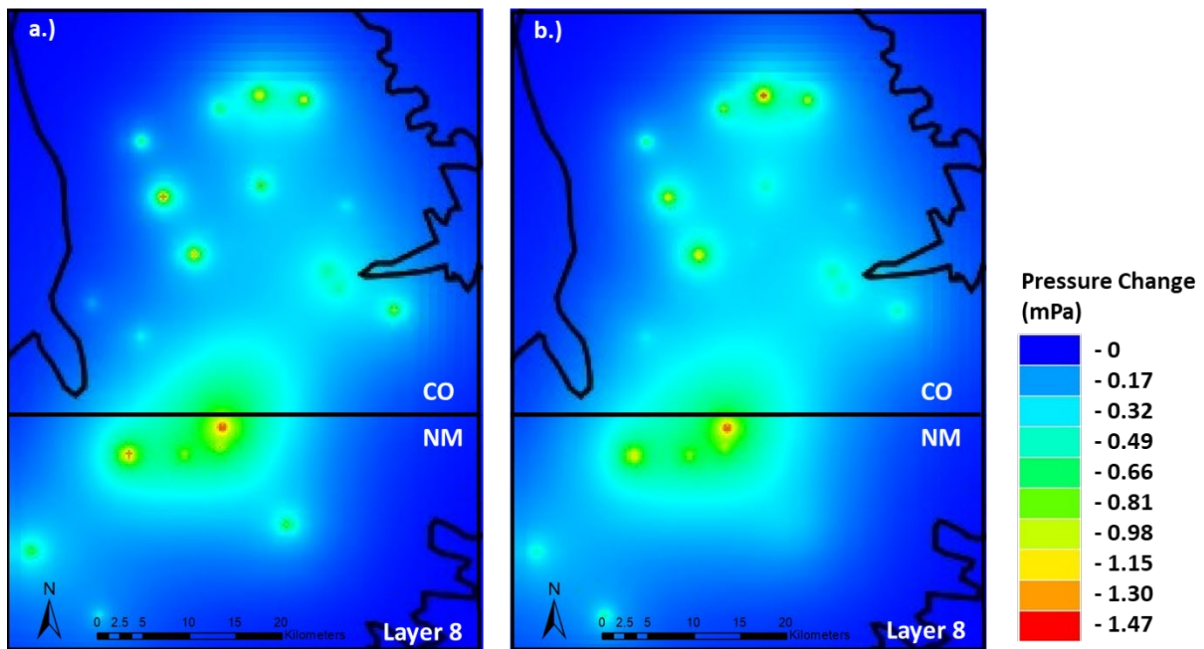


**Figure A-3:** Groundwater Model Results for pressure change distribution at 2017 (a) and 2020 (b) in layer 8.

### A.3 Surface Deformation Modeling

Using the results for hydraulic head change ( $\Delta h$ ) over time derived from the basin-scale groundwater flow model, we were able to estimate the resulting deformation observable at the ground surface. Here, we describe the methodology used to model surface deformation using results from the groundwater flow model.

Brown et al. (2022) devised a simple relationship between one dimensional vertical surface deformation to the change in hydraulic head, which can be applied to three dimensionally discretized groundwater model results. The equation is derived based on the Terzaghi (1925) principle of the coupling between sediment compaction and changes in hydraulic head applied to consolidated sedimentary rock. Recall that the relation between hydraulic head change ( $\Delta h$ ) and surface deformation is:

$$D(i, j, t) = \sum_{k=1}^N S_{S_k} b_k \Delta h_k \quad (9)$$

where  $D$  (L) is the total surface deformation as a function of the discretized model index location  $i, j$  (column, row) and time  $t$  (T), expressed as the sum of the change in vertical thickness of individual model layers  $N$  with index  $k$ .  $S_{S_k}$  is the specific storage and  $b_k$  is the vertical thickness in layer  $k$ .  $\Delta h_k$  is the hydraulic head change in layer  $k$  over time  $t$ . This equation forms the basis for the surface deformation modeling methodology in this research. Here we summarize the derivation of the equation and its relation to pore fluid pressure

perturbations and poroelastic principles. Brown et al. 2022 offers a more detailed description of the relation.

The equation for hydraulic head is represented by equation 7. As mentioned earlier, we can assume elevation head does not change with time. Thus, the change in hydraulic head throughout the domain can then be expressed solely by the pore pressure change:

$$\rho_f g \Delta h = \Delta p \quad (10)$$

where  $p$  is pore fluid pressure ( $M L^{-1}T^{-2}$ ),  $\rho$  is fluid density ( $ML^{-3}$ ), and  $g$  is gravitational acceleration ( $L T^{-2}$ ). Pore pressure relates to effective stress through the general equation for the effective stress tensor ( $\sigma'_{ij}$ ):

$$\sigma'_{ij} = \sigma_{ij} - \delta_{ij}p \quad (11)$$

where  $\sigma_{ij}$  ( $M L^{-1}T^{-2}$ ) is the total stress tensor, and  $\delta_{ij}$  is the Kronecker delta (where  $\delta_{ij} = 1$  if  $i = j$  and  $\delta_{ij} = 0$  if  $i \neq j$ ). When only considering the vertical component ( $zz$ ), the equation becomes:

$$\sigma'_{zz} = \sigma_{zz} - p \quad (12)$$

Assuming the vertical total stress ( $\sigma_{zz}$ ) does not change with time and changes in fluid density caused by compression and expansion of water are negligible, we can relate the change of effective vertical stress  $\Delta\sigma'_{zz}$  by the change in hydraulic head  $\Delta h$  (L):

$$\Delta\sigma'_{zz} = -\rho_f g \Delta h \quad (13)$$

Material compressibility ( $\alpha_m$ ) can be expressed in terms of the change in volume and stress by

$$\alpha_m = \frac{-\frac{\Delta V}{V}}{\Delta\sigma'} \quad (14)$$

where  $\alpha_m$  ( $L T^2 M^{-1}$ ) is the compressibility of the material,  $\Delta V$  ( $L^3$ ) is the change in volume,  $V$  ( $L^3$ ) is the initial volume of the material, and  $\Delta\sigma$  ( $M L^{-1} T^{-2}$ ) is the change in effective stress. Here, we only consider deformation in the vertical direction, so equation 14 can be written as

$$\overline{\alpha_m} = \frac{-\frac{\Delta b}{b}}{\Delta\sigma'_{zz}} \quad (15)$$

where  $\overline{\alpha_m}$  ( $L T^2 M^{-1}$ ) is the vertical compressibility of the medium,  $b$  ( $L$ ) is the starting thickness, and  $\Delta b$  ( $L$ ) is the change in material thickness. The relation assumes that changes in effective stress are entirely due to pore pressure perturbations. Therefore, equations 13 and 15 is combined:

$$\rho_f g \overline{\alpha_m} b = \frac{\Delta b}{\Delta h} \quad (16)$$

The equation for specific storage ( $S_s$ ) as a function of rock compressibility ( $\alpha_m$ ) is

$$S_s = \rho_f g (\alpha_m + n\beta) \quad (17)$$

where  $n$  is porosity [1] of the aquifer material and  $\beta$  is the compressibility of water ( $L T^2 M^{-1}$ ).

Typically, the product of porosity ( $n$ ) and the compressibility of water ( $\beta$ ) is negligible compared to the compressibility of the rock material ( $\alpha_m$ ). There are some lithologies where

$\alpha_m < n\beta$  (Freeze and Cherry 1979). However, as Brown et al. 2022 notes, these specific

lithologies are unlikely to be within the injection intervals in sedimentary rock formations.

Therefore, equation 17 is substituted into equation 16 to express the change in thickness ( $\Delta b$ )

(L) with respect to the change in hydraulic head ( $\Delta h$ ):

$$\Delta b = S_s b \Delta h \quad (18)$$

Equation 17 is used to calculate the change in thickness of each cell within the discretized groundwater model domain. Summing the deformation in each cell within a vertical column of cells at every column and row combination results in the deformation observable at the land surface (equation 9).

When calculating the surface deformation using equation 9, several assumptions must be made (Brown et al. 2022). One assumption is that deformation is entirely elastic. This means that deformation is not permanent and will respond linearly to pore pressure changes. In other words, when pore pressure increases or decreases, the rock will deform. But when the stress is removed from the system, the medium will return to its original volume. Inelastic deformation

on the other hand, occurs when the deformation is permanent due to the irreversible compaction and reorganization of grains within compressible clay and silt interbeds (Poland and Davis, 1969; Schmidt and Bürgmann, 2003). Inelastic deformation is typically observed where excess groundwater pumping results in the compaction of sediments that were previously saturated (Schmidt and Bürgmann, 2003). With inelastic cases, after subsidence occurs, the porous medium will lose some of its ability to expand. It is possible that both forms of deformation occurs within the subsurface in the Raton Basin, but because wastewater injection increases the pore pressure within the injection interval (and does not decrease pressure beneath pre-injection levels) and no production occurs within the injection formation, deformation due to wastewater injection is likely predominantly elastic. Another assumption is that deformation is instantaneous. Delays in surface deformation can occur due to the presence of clay lenses within the aquifer, which are inconsistent with deep permeable aquifers where fluid is injected (Brown et al., 2022). Time delays are considered negligible in this research. A third assumption is that the deformation is entirely vertical. We would expect that deformation in the vertical direction would have less resistance than deformation in the horizontal direction. Thus, we can assume that deformation occurs predominantly in the vertical direction.

Regional-scale surface deformation maps were created by applying equation 18 for every cell in the groundwater flow model, then equation 9 for every  $i, j$  (column/row) combination within the model domain (**Figure A-4**).

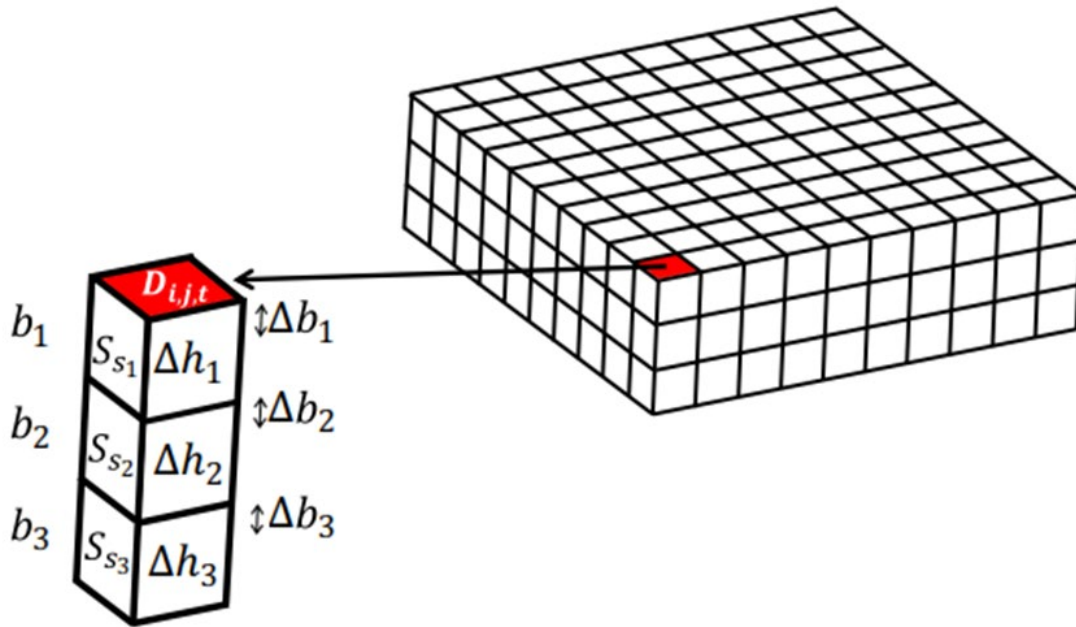


**Figure A-4:** Diagram depicting the method of calculating surface deformation using groundwater model results for hydraulic head (from Brown et al., 2022). Cumulative vertical deformation is calculated by summing the change in thickness  $\Delta b_k$  for each cell in a vertical column of cells. The change in thickness of a cell is derived by the product of the change in head  $\Delta h_k$ , initial cell thickness  $b_k$ , and the specific storage  $S_{S_k}$ .

Due to the variability of surface terrain and hydrostratigraphic unit elevations, each of the several million nodes in each  $i, j$  combination and different modeled hydrostratigraphic unit has a unique thickness. The thicknesses for each node  $b_k$  was calculated using a python algorithm. The calculated thickness of each node can be expressed by the following equation:

$$b_{i,j,k} = \frac{z_{l_{i,j}} - z_{(l+1)_{i,j}}}{d_l} \quad (19)$$

where  $z_{l_{i,j}}$  (L) is the elevation of top of model unit  $l$  at column and row index  $(i, j)$ ,  $z_{(l+1)_{i,j}}$  is the top elevation (L) of unit  $l + 1$  (underlying unit) at column and row index  $(i, j)$ , and  $d_l$  is the number of discretized nodes within the model unit. The top elevations of each model unit at each  $i, j$  was extracted from the layer definition dataset used in the MODFLOW-2005 groundwater model development.

Specific storage  $S_{S_k}$  is an intrinsic property of the aquifer material in layer  $k$ . In our model, the specific storage of the upper aquifer is  $1.0 \times 10^{-5}$ . The specific storage of the upper aquifer was assigned to all  $i, j, k$  combinations where the layer index is less than or equal to the number of discretized nodes in the top layer:

$$S_{S_k} = 1.0 \times 10^{-5} \text{ if } k \leq d_{l_1} \quad (20)$$

while the specific storage for the middle aquifer (injection zone) is  $1.0 \times 10^{-6}$

$$S_{S_k} = 1.0 \times 10^{-6} \text{ if } d_{l_1} \leq k \leq d_{l_2} \quad (21)$$

and the specific storage for the basement is  $1.0 \times 10^{-7}$

$$S_{S_k} = 1.0 \times 10^{-7} \text{ if } k \geq d_{t_2} \quad (22)$$

A crucial element when calculating deformation is the change in hydraulic head ( $\Delta h$ ). MODFLOW-2005 calculates the distribution of head a specified time step. The distribution of hydraulic head for November 1994 (pre-injection), 2017, 2018, 2019, and 2020, respectively, were exported from the groundwater model results. The change in hydraulic head for each node within the study area  $\Delta h_{i,j,k}$  over a specified time  $t$  was calculated by subtracting groundwater flow model results for hydraulic head between the two time periods of interest:

$$\Delta h_{i,j,k} = h_{i,j,k,t_2} - h_{i,j,k,t_1} \quad (23)$$

where  $h_{i,j,k,t_2}$  is hydraulic head at cell  $i, j, k$  at time  $t_2$ , and  $h_{i,j,k,t_1}$  is hydraulic head at cell  $i, j, k$  at time  $t_1$ .

With the change in hydraulic head, node thickness, and specific storage determined for every combination of  $i, j, k$  in the study area, the surface deformation  $D$  was calculated for each column, row combination using equation 9. Results for surface deformation at each column and row combination were imported into ESRI ArcMap™ as points, representing calculated cumulative deformation at each surficial node. Surface deformation maps were then created using natural neighbor interpolation in ESRI ArcMap™. Maximum uplift and subsidence, along with the extent of deformation, can readily be extracted from GIS results.

Time series for hydraulic was extracted from the groundwater model results using a MODFLOW post-processing software package GW\_Chart. For each chosen time series location  $(i, j)$ , data for hydraulic head over time was extracted for each layer  $k$ . The change in hydraulic head since wastewater injection began was calculated by subtracting the hydraulic head at the specified time step by the initial head at  $t = 0$ . Like the creation of surface uplift maps, equation 9 can be applied to the results for hydraulic head change to calculate deformation over time. The deformation calculated for each cell in a vertical column of cells is summed to estimate total surface deformation. We created five time-series (East, West, South, Northeast, and Northwest) to represent the general deformation over time within the four subregions.

## Appendix B: First-order lithospheric expansion estimation

### B.1 Coalbed Methane and Gas Production and Mining Activities

The Class II wastewater injection modeled in this study is related to extensive coalbed methane and gas production in addition to mining activities (**Figure B-1**). As such, there is an abundance of production wells operating within the Raton Basin (COGCC, 2020; NMOCD, 2020). Previous studies have observed surface deformation within oil and gas producing regions (e.g., Deng et al., 2020). Furthermore, mining operations can impact surface deformation observed using DInSAR (Menezes, 2022). We note that surface deformation due to oil and gas production can be considered negligible if the production is primarily through enhanced oil recovery (EOR) (Brown et al, 2022). EOR is the practice of injecting a nearly equal volume of fluid into the production zone to, keeping the pore pressure constant, to help facilitate additional hydrocarbon flow and increase the efficiency of production (Rubinstein and Mahani 2015; Brown et al, 2022). Fluids have been extracted from within the Raton Basin at a significant rate since the 1990s, with just the water production rate reaching a rate of over 140 million barrels a year in 2008 (**Figure B-2**). Estimating the effects of oil/gas/water production on surface deformation would likely require the development of additional models and is outside the scope of this study. However, if the goal is to model the deformation more accurately as seen on the surface, the deformation expressed by these factors can later be incorporated.

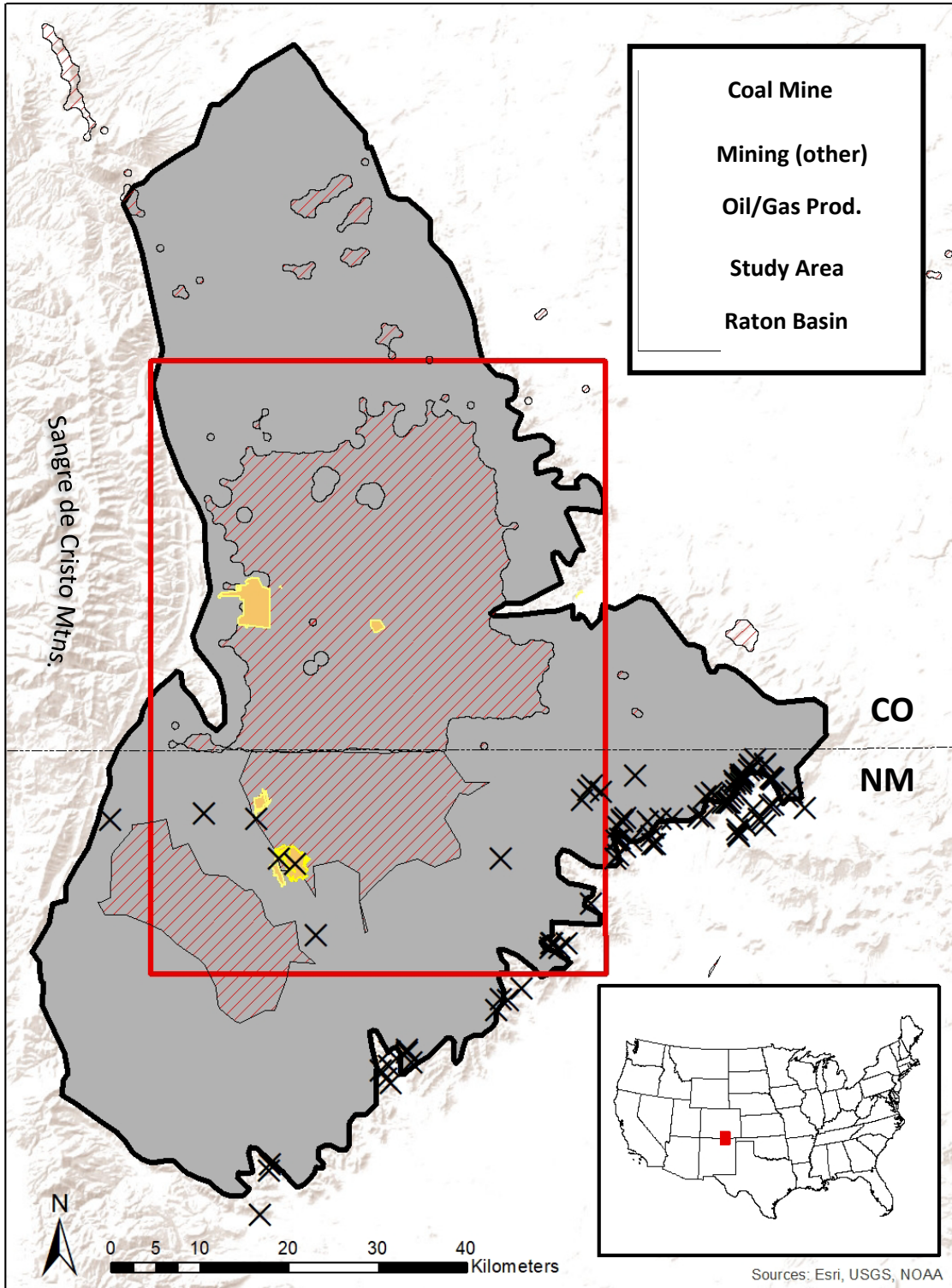


**Figure B-1:** Map of coalbed methane and gas production and mining operations within the Raton Basin (data source: Menezes 2022)

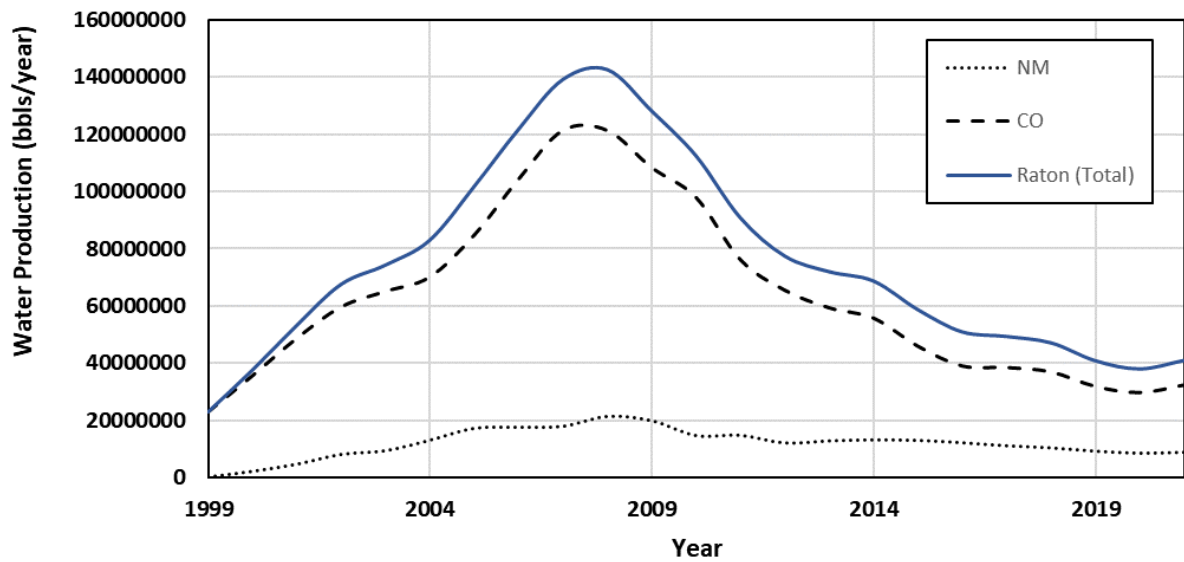


**Figure B-2:** Water Production rate (bbls/yr) for the Colorado and New Mexico portions of the Raton Basin, respectively.

## **B.2 Lithospheric Expansion Due to Groundwater Storage Depletion**

Isostatic rebound is a well-documented phenomenon in which large scale uplift of the crust occurs after a load is removed. A decrease in crustal mass causes a readjustment of regional surface elevation as the lithosphere reaches isostatic equilibrium. This phenomenon has been observed in some areas following groundwater extraction (e.g. Holzer, 1979; Amos et al., 2014). When large volumes of fluid are extracted from aquifers the overall crustal mass decreases resulting in the unburdening of the lithosphere. A recent study by Amos et al. (2014) used GPS measurements of vertical surface displacements to show that a substantial region of rock uplift up to 1-3 millimeters per year surrounding the southern San Joaquin Valley of California, region that has experienced significant groundwater extraction for agricultural use.

Groundwater is produced and extracted during coalbed methane and gas production in the Raton Basin (COGCC 2021; NMOCD, 2021), though the rate of water extraction is orders of magnitude lower than that in California's central valley related to agricultural use (Amos et al. 2014). It is possible lithospheric expansion plays a role in contributing some uplift, though the degree of uplift is uncertain and likely small. However, to quantify uplift due to lithospheric expansion, and perhaps factor this mechanism out as a significant contributor to uplift, we apply a first-order calculation for isostatic rebound following crustal unloading (Jiang et al., 2010; Amos et al., 2014).

The equation is:

$$\begin{aligned}
 U_{obs, z=0} = & \frac{(1 - \nu)N_0}{\pi G(2a)} \\
 & \times |(x_{obs} - a) \ln|x_{obs} - a| - (x_{obs} + a) \ln|x_{obs} + a| - (x_{ref} \\
 & - a) \ln|x_{ref} - a| + (x_{ref} + a) \ln|x_{ref} + a||
 \end{aligned} \tag{24}$$

where  $x_{obs}$  and  $x_{ref}$  are the horizontal locations of the uplift observation and reference points respectively,  $z$  is the vertical dimension,  $N_0$  is a rate of load decrease,  $\nu$  is Poisson's ratio,  $G$  is the shear modulus,  $a$  is the strip half-width, and  $U_{obs, z=0}$  is the surficial uplift rate observed at the observation point. A poisson's ratio of 0.25 and a Skempton Coefficient of 30 GPa was used. The top-to-bottom length of the production region was used to determine the half-width ( $a$ ). The Raton Basin produced a total of roughly 267 million cubic meters of groundwater between 1999 and 2020 (COOGC, 2021; NMOGD, 2021) which averages a rate of roughly 12 million cubic meters extracted per year. This equates to a load loss rate ( $N_0$ ) of  $8.6 \times 10^5 \text{ N m}^{-1} \text{ yr}^{-1}$ . A far-field reference point at 400,000 meters is used. An observation point a meter from the center of the line load was chosen since we'd expected the greatest amount of uplift to be concentrated in the center. The resulting first-order estimated uplift is on the order of sub-millimeters per year (estimated result:  $\sim 3.0 \times 10^{-5} \text{ m}$ ), suggesting minimal contribution of lithospheric rebound from coalbed methane and gas production to overall basin-scale uplift.

## Appendix C: Sensitivity Analysis

Hydraulic diffusivity ( $\omega$ ), describes the ability of fluid pressure to diffuse within a saturated porous medium and is a function of both the medium and fluid properties (Freeze & Cherry, 1979).

Here, we test two additional aquifer diffusivities by altering the specific storage ( $S_s$ ). Specific storage is an important parameter in calculating both pore pressure propagation and surface deformation. All scenarios (including the moderate diffusivity scenario in an early section) consider the same injection rates. Both low and high diffusivity scenarios are extreme and are unlikely to be representative of the actual hydrogeological properties of the injection unit. **Table C-1** shows the parameters used for both diffusivity scenarios.

**Table C-1:** Parameters used in sensitivity analysis.

<b>Parameters</b>	$K = 10^{-6} \text{ m/s}$
$S_s = 10^{-5} \text{ m}^{-1}$	$\omega = 0.1 \text{ m}^2/\text{s}$
$S_s = 10^{-7} \text{ m}^{-1}$	$\omega = 10 \text{ m}^2/\text{s}$

**Figure C-1** shows the surface deformation for both diffusivity scenarios. As expected, the low diffusivity scenario results in a significantly larger calculated surface deformation that is more contained to localized areas surrounding injection wells. The model predicts a maximum uplift of roughly 0.13 m occurring directly over several injection wells. The maximum subsidence is around 0.18 m directly above injection wells that had the sharpest decline in injection rates. The high diffusivity scenario results in a much more significant spread in surface deformation, encompassing most of the study area. Because of the greater extent, the magnitude of deformation in any given location is smaller. The maximum calculated uplift of 0.004 m occurs directly over a well in the north. Calculated subsidence up to around 0.004 m occurs over a southern well that experienced a significant decrease in injection rate.

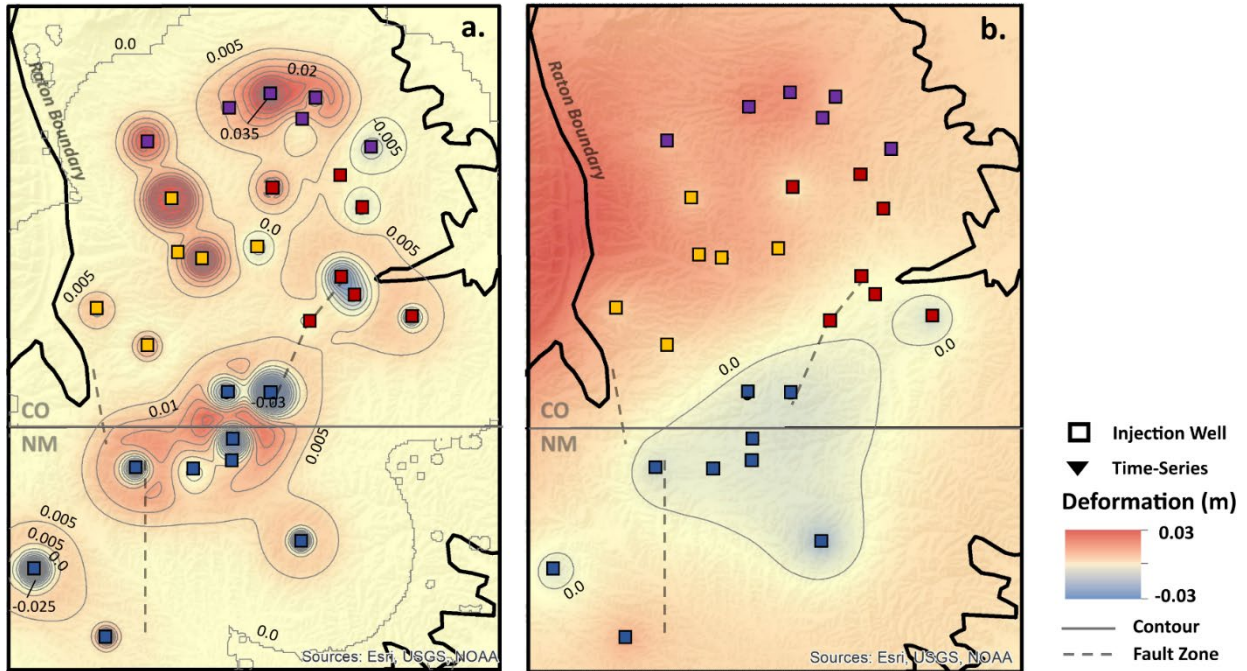


**Figure C-1.** Sensitivity analysis results for 2017-2020. **a.** shows surface deformation when specific storage is high ( $S_s = 10^{-5}$ ) and diffusivity is low ( $\omega = 0.1 \text{ m}^2/\text{s}$ ), and **b.** represents deformation when specific storage is low ( $S_s = 10^{-7}$ ) and diffusivity is high ( $\omega = 10 \text{ m}^2/\text{s}$ ). Injection wells are denoted here by small squares to allow for additional visibility of deformation surrounding injectors. Contours and red color scheme represent the calculated surface deformation measured in meters (m). Deformation in **a.** has a greater magnitude but lower spread. Deformation in **b.** has a greater spread but lower magnitude.

## Appendix D: Recent DInSAR interpretations of Surface Deformation and Future Work.

### D.1 Differential Interferometric Synthetic Aperture Radar (DInSAR)

The practice of injecting water into the subsurface for a variety of purposes has occurred in the United States since the 1930's (Clark et al., 2005), but subtle changes in surface elevation due to deep fluid injection went largely unnoticed (Teatini et al. 2011). Advancements in geodetic techniques over the past several decades have facilitated new studies measuring deformation related to injection (Teatini et al 2011) and has opened the doors to the possibility of using surface deformation as a calibration tool in groundwater modeling (Brown et al., 2022). DInSAR is a satellite imaging technique used to measure surface deformation through time with microwaves (Gabriel et al., 1989). It is useful due to its centimeter to millimeter scale accuracy, relatively fine spatial resolution, and large spatial coverage capacity allowing for regional scale data acquisition (Gabriel et al., 1989). The method of using DInSAR to measure surface displacement works by analyzing the phase difference (referred to as an interferogram) between two SAR images of a specific location taken at separate times (Gabriel et al., 1989; Lanari, 2007) (**Figure D-1**). It can be used to detect and measure singular surface displacement events such as deformation due to earthquakes (Peltzer and Rosen, 1995) as well as to analyze the temporal evolution of surface deformation using time-series (Schmidt & Bürgmann, 2003; Notti et al, 2015; Shirzaei et al. 2016). DInSAR has proven to be a useful tool in measuring surface displacements related to Class II wastewater injection (e.g. Shirzaei et al., 2016; Barba-Sevilla et al. 2018; Kim and Lu 2018; Loesch and Sagan 2018; Brown et al., 2022). For instance,

Shirzaei et al. 2016 measured surface uplift related to groundwater injection in eastern Texas, and related deformation to areas of elevated seismic hazard.

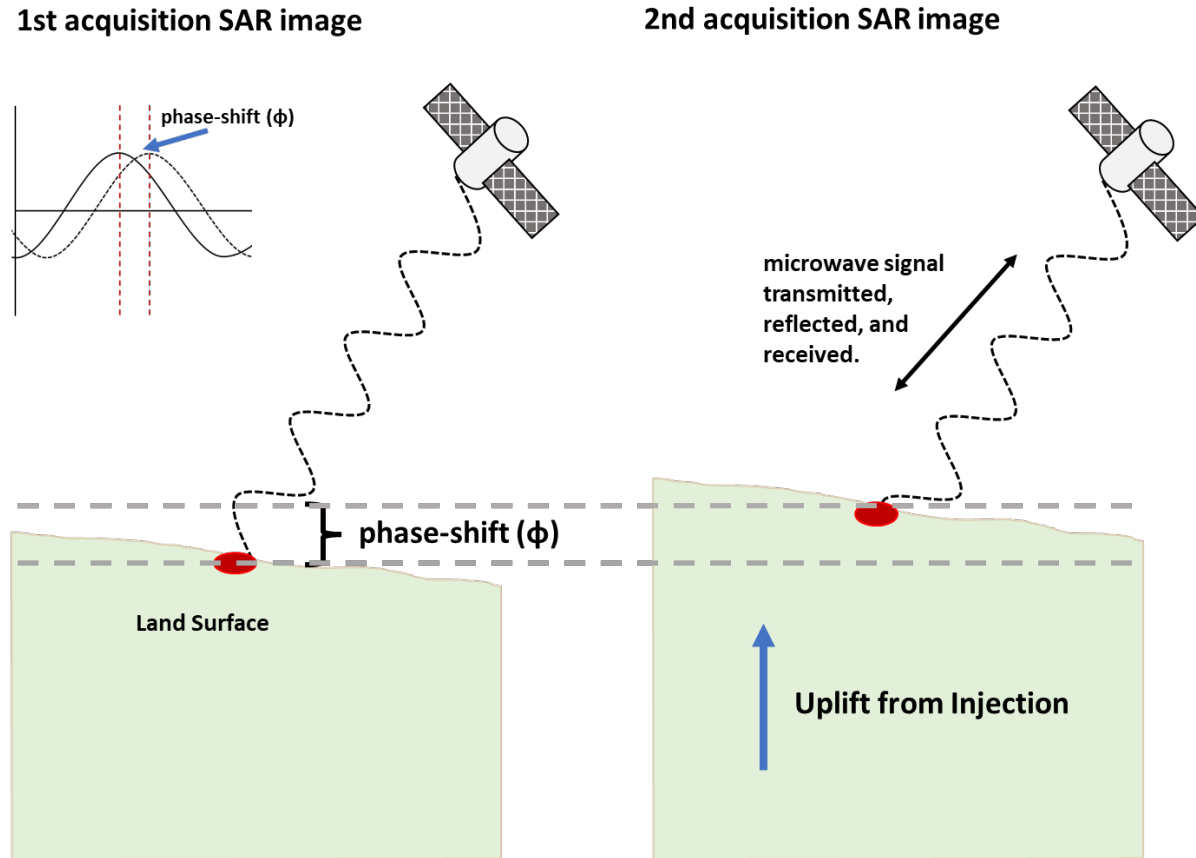


**Figure D-1:** Conceptual diagram depicting Differential Interferometric Synthetic Aperture Radar (DInSAR) measurements of surface displacements due to injection. The figure is inspired by Schindler et al., 2019. Synthetic Aperture Radar (SAR) works by transmitting microwave signal and determining the phase of the reflected signal. The DInSAR method is applied by measuring the difference in wave phases between two separate image acquisitions at different times. The change in wave phase is used to estimate surface displacements through time.

However, there are potential sources of error associated with using DInSAR to measure surface deformation. A common error when processing DInSAR data is the occurrence of noise, often referred to as decorrelation phenomena (Zebker and Villasenor, 1992; Lanari et al., 2007). There is typically lower decorrelation in rocky, dry, or urbanized areas but higher decorrelation

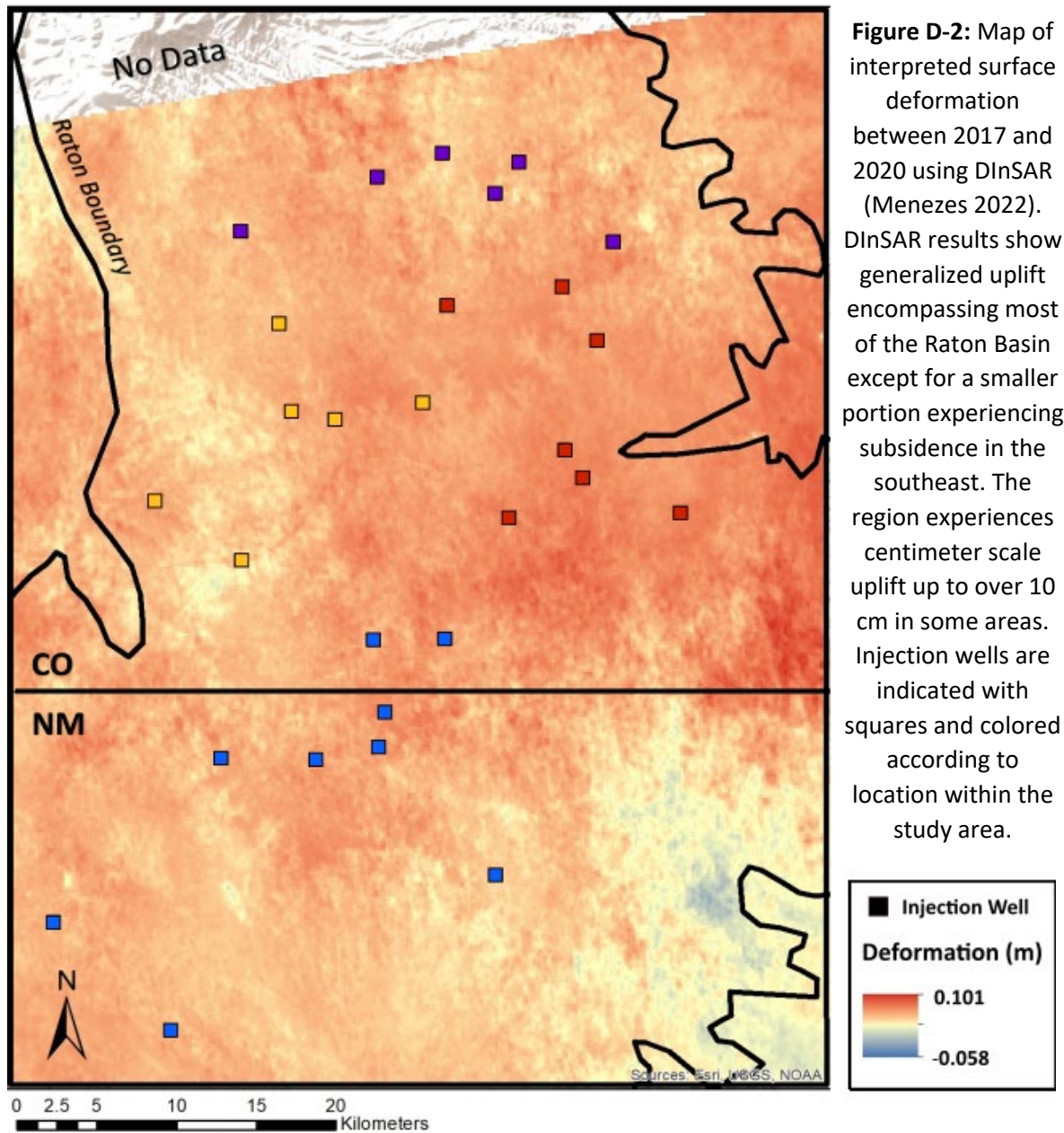
in areas with heavy vegetation, agricultural activity, snow, and water (Rosen et al. 2000; Lanari et al., 2007). When looking at vertical deformation, measurements of lateral motion on the land surface would need to be removed, often using models or limited data which creates uncertainty in the results (Massonnet and Feigl 1998).

## **D.2 Interpreted surface deformation in the Raton Basin using DInSAR**

Surface deformation through time has previously been inferred within the Raton Basin. Menezes (2022) used the DInSAR geodetic technique applied to Synthetic aperture radar (SAR) data gathered by the European Space Agency's C-band Sentinel-1B satellite between 2017-2021. A basin scale map of deformation between 2017 and 2020 was created using the data (**Figure D-2**). The study found a generalized centimeter scale increase in surface elevation, up to 10 centimeters, encompassing most of the basin. A smaller portion of the study area in the southeast saw subsidence up to nearly 6 cms. Furthermore, the study found that the land surface surrounding low-volume injection wells follow similar patterns and rates of uplift as the land surface surrounding high-volume injectors.

If the uplift is primarily due to wastewater injection, that would require high aquifer diffusivities allowing for the rapid basin-wide spread of pore pressure, while simultaneously being sufficiently contained such that pressure builds up and significantly deforms the rock material. As shown by the sensitivity analysis in a previous section, low diffusivity implies greater but localized deformation while high pressure diffusion implies less deformation covering larger areas. The pore fluid pressure increase required to cause basin-scale uplift up to 10cm is astronomical. The pressure increases due to injection between 2017-2020 is likely

insufficient to cause surface displacements of that scale. Additional, not-yet-identified mechanisms must be also responsible for causing the basin-extending, centimeter scale uplift.



### **D.3 Future work: Pore Pressure Model Calibration using DInSAR Interpretations**

The intersection between geodetic measurements of surface deformation and modeled pore pressure distribution has garnered recent interest. Measured deformation may be useful in calibrating deep stratigraphy pore pressure models where in situ measurements of hydrogeologic properties are scarce. Advancements in geodetic techniques over the past several decades have facilitated new studies measuring deformation related to injection (Teatini et al 2011) and has opened the doors to the possibility of using surface deformation as a calibration tool in groundwater modeling (Brown et al., 2022). We propose that our modeling methodology can be combined with DInSAR interpretations to calibrate deep stratigraphy pore pressure models related to fluid injection. Calculated results can be matched to interpreted deformation using DInSAR to constrain hydrogeologic parameters. This technique would entail altering pore pressure and surface deformation model parameters until calculated results are reasonably like interpreted DInSAR results. Due to the model's sensitivity to storativity ( $s$ ), we suggest that it is constrained using this technique. However, hydraulic conductivity ( $k$ ) can also be constrained. DInSAR measures total surface deformation related to possibly many mechanisms in addition to fluid injection. It cannot determine the magnitude or extent of deformation related to any specific process unless other processes are factored out.

Deformation mechanisms, such as additional anthropogenic activities, erosional processes such as landslides (e.g. Notti et al., 2015), earthquake slip (e.g. Atzori et al., 2009, Barnhart et al., 2014), and aseismic creep (e.g. Tiampo, 2013) can impact DInSAR results. A common error when processing DInSAR data is the occurrence of noise, often referred to as decorrelation

phenomena (Zebker and Villasenor, 1992, Lanari et al., 2007). There is typically lower decorrelation in rocky, dry, or urbanized areas but higher decorrelation in areas with heavy vegetation, agricultural activity, snow, and water (Rosen et al. 2000, Lanari et al., 2007). Decorrelation error and deformation related to additional mechanisms should both be considered and factored out before use in pore pressure model calibration.

## Appendix E: Additional Data Tables

**Table E-1: Injection Well Information**

Well Name	API		Date of IJ	Year	State
APACHE CANYON #10-3	071-06126	TIMBER CREEK OPERATING LLC	Jan-95	1995	CO
APACHE CANYON #19-10	071-06123	TIMBER CREEK OPERATING LLC	Jan-95	1995	CO
BEARDON #24-15 WD	071-07016	EVERGREEN NATURAL RESOURCES LLC	Jan-01	2001	CO
CIMARRON #32-18 WD	071-07565	EVERGREEN NATURAL RESOURCES LLC	Mar-05	2005	CO
COTTONTAIL PASS DISPOSAL WELL #32-33	071-06106	EVERGREEN NATURAL RESOURCES LLC	Nov-94	1994	CO
DEL AGUA #44-2 WD	05-071-07706	EVERGREEN NATURAL RESOURCES LLC	Jul-05	2005	CO
FERMINIA #12-6 WD	071-08889	EVERGREEN NATURAL RESOURCES LLC	Sep-07	2007	CO
HILL RANCH DEEP #14-12 WD	071-07455	EVERGREEN NATURAL RESOURCES LLC	Jul-05	2005	CO
JAROSA #32-33 WD	05-071-08532	EVERGREEN NATURAL RESOURCES LLC	May-07	2007	CO
LA GARITA #42-20 WD	071-07045	EVERGREEN NATURAL RESOURCES LLC	Aug-01	2001	CO
LONG CANYON #43-12 WD	071-07035	EVERGREEN NATURAL RESOURCES LLC	Apr-01	2001	CO
LOPEZ CANYON SWD #1	071-09733	TIMBER CREEK OPERATING LLC	Sep-10	2010	CO
PCW #12-4 WD	071-06421	EVERGREEN NATURAL RESOURCES LLC	Jul-97	1997	CO

POLLY #23-29 WD R	071- 09728	EVERGREEN NATURAL RESOURCES LLC	Jul-09	2009	CO
San Pablo #11-4 WD	071- 09916	EVERGREEN NATURAL RESOURCES LLC	Dec-14	2014	CO
SAWTOOTH #34- 4 WD	071- 06706	EVERGREEN NATURAL RESOURCES LLC	Apr-00	2000	CO
SOUTHPAW #33- 36 WD	071- 09594	EVERGREEN NATURAL RESOURCES LLC	Apr-09	2009	CO
VPR C #14 WDW	05-071- 06867	WAPITI OPERATING LLC	Sep-99	1999	CO
VPR C #204 WDW	071- 09838	WAPITI OPERATING LLC	Mar-12	2012	CO
VPR C #39	071- 06946	WAPITI OPERATING LLC	May-00	2000	CO
WESTON #24-23 A WD	071- 07690	EVERGREEN NATURAL RESOURCES LLC	Jan-04	2004	CO
WILD BOAR #21- 32 WD	071- 06741	EVERGREEN NATURAL RESOURCES LLC	Aug-00	2000	CO
El Paso VPR A 007	30-007- 20116	WAPITI OPERATING LLC	Oct-99	1999	NM
El Paso VPR A 042	30-007- 20143	WAPITI OPERATING LLC	May-00	2000	NM
El Paso VPR A 182	30-007- 20540	WAPITI OPERATING LLC	Sep-05	2005	NM
El Paso VPR A 500	30-007- 20892	WAPITI OPERATING LLC	Jun-08	2008	NM
El Paso VPR B 027	30-007- 20161	WAPITI OPERATING LLC	Jul-00	2000	NM
El Paso VPR D 025	30-007- 20152	WAPITI OPERATING LLC	Sep-00	2000	NM
El Paso VPR E 099	30-007- 20378	WAPITI OPERATING LLC	Jan-03	2003	NM

**Table E-2: Injection Well Coordinates**

Well Name	Long (UTM)	Lat (UTM)	Lat	Long
APACHE CANYON #10-3	501228	4106309	37.1031	- 104.986
APACHE CANYON #19-10	506604	4102496	37.0687	- 104.926
BEARDON #24-15 WD	529887	4123018	37.2532	- 104.663
CIMARRON #32-18 WD	506603	4123633	37.2592	- 104.926
COTTONTAIL PASS DISPOSAL WELL #32-33	519504	4118880	37.2162	-104.78
DEL AGUA #44-2 WD	522613	4126083	37.2811	- 104.745
FERMINIA #12-6 WD	515169	4127151	37.2909	- 104.829
HILL RANCH DEEP #14-12 WD	523447	4105201	37.0928	- 104.736
JAROSA #32-33 WD	519233	4128706	37.3048	- 104.783
LA GARITA #42-20 WD	518002	4112655	37.1601	- 104.797
LONG CANYON #43-12 WD	534166	4105584	37.0959	- 104.616
LOPEZ CANYON SWD #1	509785	4112042	37.1547	-104.89
PCW #12-4 WD	528140	4107801	37.1161	- 104.683
POLLY #23-29 WD R	526751	4120142	37.2274	- 104.698
San Pablo #11-4 WD	509004	4117766	37.2063	- 104.899
SAWTOOTH #34-4 WD	528913	4116658	37.1959	- 104.674
SOUTHPAW #33-36 WD	523995	4128169	37.2998	- 104.729
VPR C #14 WDW	519466	4097472	37.0232	- 104.781
VPR C #204 WDW	514894	4097415	37.0228	- 104.833

VPR C #39	519324	4097479	37.0233	- 104.783
WESTON #24-23 A WD	512459	4111591	37.1506	-104.86
WILD BOAR #21-32 WD	526905	4109684	37.1331	- 104.697
El Paso VPR A 007	515248	4090514	36.9606	- 104.829
El Paso VPR A 042	511271	4089720	36.9535	- 104.873
El Paso VPR A 182	515643	4092778	36.981	- 104.824
El Paso VPR A 500	522591	4082293	36.8863	- 104.746
El Paso VPR B 027	502241	4072291	36.7964	- 104.975
El Paso VPR D 025	494872	4079299	36.8596	- 105.058
El Paso VPR E 099	505421	4089785	36.9541	- 104.939

**Table E-3: Earthquake Data**

time	latitude	longitude	depth	mag
1995-07-04T03:59:04.530Z	36.246	-104.814	5	3.8
1996-08-01T05:44:22.750Z	37.398	-104.247	5	3.8
1996-11-01T03:09:28.350Z	37.349	-104.232	5	3.2
2001-08-28T14:16:09.520Z	37.088	-104.692	5	3.4
2001-08-28T14:22:00.330Z	37.091	-104.655	5	3.5
2001-09-04T12:22:44.970Z	37.107	-104.622	5	3.4
2001-09-04T12:45:53.220Z	37.143	-104.65	5	4
2001-09-05T10:52:07.890Z	37.143	-104.618	5	4.5
2001-09-05T14:48:58.260Z	37.112	-104.611	5	3.7
2001-09-06T09:41:43.590Z	37.11	-104.628	5	3.6

2001-09-06T11:28:26.490Z	37.14	-104.585	5	3.5
2001-09-10T18:56:00.370Z	37.108	-104.602	5	3.4
2001-09-13T16:39:05.440Z	37.091	-104.593	5	3
2001-09-21T19:10:59.670Z	37.121	-104.706	5.4	3.4
2001-12-15T07:58:31.360Z	36.859	-104.797	5	3.3
2002-01-26T01:06:03.860Z	36.86	-104.784	5	3.4
2002-06-18T09:12:36.660Z	36.881	-104.779	5	3.5
2002-11-14T04:56:52.260Z	36.917	-104.768	5	3.2
2002-12-31T19:02:29.660Z	36.972	-104.774	0	3.9
2003-04-28T07:32:26.040Z	36.844	-104.923	5	3.6
2003-06-03T18:09:27.840Z	36.994	-104.768	5	3.3
2003-06-15T00:22:17.970Z	36.91	-104.763	5	3.6
2003-08-14T00:11:08.960Z	36.945	-104.87	5	3.3
2003-09-08T11:02:49.310Z	37.369	-104.685	5	3
2003-09-13T15:22:40.990Z	36.831	-104.907	5	3.8
2003-11-24T07:05:57.720Z	36.958	-104.828	5	3.1
2003-12-28T02:55:02.320Z	37.596	-105.28	5	3.5
2003-12-28T03:57:03.210Z	37.584	-105.298	5	3.1
2004-02-03T14:34:22.570Z	36.932	-104.861	5	3.4
2004-03-22T12:09:56.460Z	36.855	-104.851	5	4.4
2004-03-30T01:02:55.400Z	36.892	-104.876	5	3

2004-03-30T02:23:37.860Z	36.876	-104.831	5	3.1
2004-03-30T02:41:04.150Z	37.036	-104.931	5	3.5
2004-05-31T03:27:43.770Z	36.935	-104.835	5	3.3
2004-08-01T06:50:47.630Z	36.874	-105.104	5	4.3
2005-01-10T10:14:59.150Z	37.007	-104.675	5	3.4
2005-04-24T11:02:35.900Z	36.92	-105.07	5	3.4
2005-07-04T10:45:24.500Z	36.86	-105.097	5	3
2005-07-08T06:24:01.120Z	36.938	-104.886	5	3
2005-08-10T22:08:16.960Z	36.952	-104.822	5	4.1
2005-08-10T22:08:22.610Z	36.947	-104.833	5	5
2005-08-10T22:24:33.940Z	36.982	-104.959	5	3
2005-10-20T08:15:36.580Z	36.97	-104.849	5	3
2006-01-27T18:48:49.230Z	37.03	-104.968	5	3.3
2006-05-06T17:07:01.340Z	37.014	-104.768	5	3.1
2006-05-26T06:14:25.120Z	36.795	-104.832	5	3.1
2006-07-11T11:53:37.780Z	36.964	-104.929	5	3.2
2006-08-24T14:04:25.880Z	37.014	-105.013	5	3.1
2006-09-09T09:54:06.650Z	37.296	-104.77	5	3.2
2006-09-09T12:53:14.210Z	37.368	-104.865	5	3
2006-09-09T23:14:35.540Z	37.298	-104.794	5	3.6
2006-09-14T13:03:24.260Z	37.01	-104.867	5	3

2006-10-30T02:35:13.470Z	36.811	-104.963	5	3.5
2006-11-24T23:22:24.100Z	37.04	-104.996	5	3.1
2006-12-24T11:50:21.470Z	36.935	-104.75	5	3.6
2007-01-03T14:34:38.540Z	37.067	-104.895	5	4.4
2007-01-14T05:17:36.690Z	36.878	-104.93	5	3.2
2007-02-25T11:24:19.150Z	37.099	-104.773	5	3.1
2007-03-12T06:32:14.590Z	37.061	-104.937	5	3.4
2007-06-09T10:45:44.710Z	36.929	-104.793	1	3.3
2008-01-29T02:30:24.320Z	36.871	-104.988	5	3.1
2008-04-21T09:36:29.910Z	37.158	-104.942	5	3.2
2008-04-24T02:21:51.440Z	37.032	-104.847	5	3.1
2008-08-24T22:48:31.500Z	37.095	-104.866	5	3.4
2008-09-25T16:55:35.280Z	37.357	-104.882	5	3.2
2008-10-04T12:41:20.900Z	37.263	-104.748	5	3.4
2009-02-03T23:27:10.330Z	36.992	-104.884	5	3
2009-03-22T11:14:40.100Z	37.261	-104.462	5	3
2009-05-01T01:34:03.870Z	36.818	-104.819	5	3.2
2009-06-27T06:44:39.910Z	36.888	-104.906	5	3
2009-07-29T10:00:36.710Z	36.799	-104.831	5	4.1
2009-09-29T11:20:27.800Z	37.055	-104.995	5	3.1
2009-09-29T22:54:07.480Z	37.003	-104.805	5	3.5

2009-10-03T18:45:31.860Z	37.022	-104.855	5	3.6
2009-11-20T14:54:30.110Z	36.892	-104.987	5	3.7
2009-12-11T20:32:27.160Z	36.927	-105.03	5	3.2
2010-01-18T08:41:07.370Z	36.854	-104.819	5	3.8
2010-04-08T09:36:57.390Z	36.916	-104.842	5	3.5
2010-05-27T19:43:11.060Z	37.012	-104.906	5	3.6
2011-02-13T11:44:52.640Z	37.005	-104.935	5	3.6
2011-03-12T04:16:05.630Z	36.861	-104.981	5	3.2
2011-05-09T23:28:52.800Z	37.021	-104.783	5	3.7
2011-05-11T19:06:15.280Z	37.1	-104.665	5	3.8
2011-08-22T23:30:19.870Z	37.032	-104.554	5	4.7
2011-08-23T02:48:51.040Z	37.023	-104.667	5	3
2011-08-23T05:46:18.250Z	37.063	-104.701	4	5.3
2011-08-23T06:56:58.510Z	37.113	-104.631	5	3.5
2011-08-23T07:01:34.140Z	37.105	-104.679	5	3.2
2011-08-23T07:17:58.260Z	37.101	-104.63	5	3.5
2011-08-23T09:37:56.820Z	37.068	-104.764	5	3.2
2011-08-23T14:11:12.820Z	37.055	-104.692	5	4
2011-08-24T07:15:57.330Z	37.129	-104.803	5	3
2011-08-25T03:44:38.420Z	37.123	-104.697	5	3.2
2011-09-13T01:37:18.530Z	36.94	-104.798	5	3.5

2011-09-13T05:24:39.620Z	36.933	-104.741	5	4
2011-09-16T14:51:51.290Z	36.884	-104.74	5	3.9
2011-10-10T13:26:29.200Z	37.09	-104.688	5	3.2
2011-11-22T14:20:02.890Z	37.003	-104.956	5	3.4
2011-12-09T03:54:15.770Z	37.099	-104.656	5	3.4
2011-12-17T03:16:49.260Z	37.043	-104.913	5	3
2012-03-06T13:10:21.660Z	37.002	-104.925	5	3.3
2012-05-24T05:44:37.600Z	37.123	-104.743	5	3.2
2012-09-16T23:15:30.640Z	37.057	-104.916	5	3
2012-12-04T15:15:26.800Z	37.033	-104.938	5	3.5
2012-12-13T19:05:51.800Z	36.967	-104.813	5	3.3
2013-04-20T06:47:15.920Z	36.973	-104.875	5	3
2013-09-08T08:15:31.100Z	36.9651	-104.876	5	3.6
2014-01-22T18:45:03.990Z	37.2279	-104.642	4.37	3.6
2014-04-11T10:47:45.560Z	37.1499	-104.943	5.16	3.2
2014-04-16T16:03:46.500Z	37.1061	-104.801	5	3.2
2014-07-10T03:22:47.640Z	37.0008	-104.967	3.91	3.1
2014-10-10T22:57:21.930Z	37.0836	-104.904	1.36	3.3
2014-10-17T17:01:05.430Z	37.0163	-104.922	4.6	3.8
2014-10-24T12:50:47.750Z	36.9972	-104.923	5	3.3
2014-11-02T13:16:18.690Z	37.0753	-104.912	6.07	3

2014-12-02T21:57:20.310Z	37.1054	-104.939	2.99	3
2014-12-23T12:33:36.450Z	36.9501	-104.772	8.59	3.4
2014-12-27T08:23:24.760Z	37.0159	-104.849	3.51	3
2015-01-07T00:40:26.570Z	36.8765	-104.751	4.33	3.7
2015-01-20T13:53:20.700Z	36.8765	-105.007	0	3.3
2015-02-02T14:10:12.970Z	37.0845	-104.975	5	3.1
2015-02-22T07:31:48.140Z	37.1555	-104.982	5	3.6
2015-02-22T08:20:34.750Z	37.0503	-104.951	5	3.6
2015-03-05T14:49:01.270Z	36.9461	-104.899	2.52	3.4
2015-03-07T08:59:34.950Z	37.0719	-104.938	1.17	3.5
2015-03-14T20:17:30.590Z	36.9028	-104.777	1.64	3.6
2015-03-20T05:19:18.920Z	36.8932	-104.746	5	3.8
2015-08-20T05:14:09.560Z	37.1001	-104.921	1.08	3.9
2015-12-29T12:25:32.470Z	37.1308	-104.913	5	3
2016-01-15T01:54:55.190Z	36.928	-104.771	7.59	3
2016-02-03T14:59:19.110Z	37.1533	-104.954	3.13	3.3
2016-02-06T23:09:10.990Z	37.0868	-104.957	1.57	4
2016-05-21T20:51:16.840Z	36.9398	-104.811	2.3	3.2
2016-08-23T16:56:11.540Z	36.9863	-104.945	3.6	3.9
2016-11-06T04:48:35.770Z	36.9233	-104.889	1.49	3.2
2016-12-23T19:31:12.960Z	36.7571	-104.928	3.55	4.2

2017-01-21T03:57:54.300Z	36.9566	-104.843	6.27	3.1
2017-06-11T08:58:55.740Z	37.0539	-104.978	5	3.1
2017-06-17T06:42:07.660Z	37.0349	-104.898	2.16	3.5
2017-09-08T06:53:34.760Z	36.9956	-104.951	6.27	3.6
2017-09-10T08:34:41.960Z	37.0369	-104.955	5	3.7
2017-10-10T23:31:45.400Z	37.041	-104.903	5.93	3.4
2017-12-20T04:41:41.080Z	37.2887	-104.927	2.12	3.4
2017-12-30T23:46:11.940Z	37.2734	-104.863	4	4
2018-01-28T21:23:17.120Z	36.7984	-104.969	5	3
2018-02-25T06:51:17.660Z	37.2387	-104.821	5	3.5
2018-07-03T21:16:08.620Z	36.9661	-104.861	8.1	3.1
2018-08-24T06:56:52.040Z	36.9477	-104.854	6.8	3.6
2018-08-24T07:59:19.440Z	36.9806	-104.862	7.94	3.3
2018-12-26T00:25:48.560Z	36.7135	-104.984	5	3.6
2019-03-11T11:44:15.937Z	37.0182	-104.796	5	3.1
2019-05-19T10:43:18.704Z	37.0193	-104.991	5.06	3.8
2019-05-22T03:55:39.339Z	37.0181	-104.982	5	3.1
2019-09-01T11:29:43.342Z	37.2661	-104.918	4.76	3.5
2019-09-08T07:33:07.659Z	36.8895	-104.868	5	3.1
2019-11-30T07:02:08.164Z	37.0044	-105.005	8.17	3.1